219

Linear dynamics of wind waves in coupled turbulent air–water flow. Part 2. Numerical model

By J. A. HARRIS[1]† S. E. BELCHER[2]‡ AND R. L. STREET[1]

[1]Environmental Fluid Mechanics Laboratory, Stanford University,
Stanford, CA 94305-4020, USA

[2]Department of Applied Mathematics and Theoretical Physics, University of Cambridge,
Silver Street, Cambridge CB3 9EW, UK

We develop a numerical model of the interaction between wind and a small-amplitude water wave. The model first calculates the turbulent flows in both the air and water that would be obtained with a flat interface, and then calculates linear perturbations to this base flow caused by a travelling surface wave. Turbulent stresses in the base flow are parameterized using an eddy viscosity derived from a low-turbulent-Reynolds-number $k - \varepsilon$ model. Turbulent stresses in the perturbed flow are parameterized using a new *damped eddy viscosity model*, in which the eddy viscosity model is used only in inner regions, and is damped exponentially to zero outside these inner regions. This approach is consistent with previously developed physical scaling arguments. Even on the ocean the interface can be aerodynamically smooth, transitional or rough, so the new model parameterizes the interface with a roughness Reynolds number and retains effects of molecular stresses (on both mean and turbulent parts of the flow).

The damped eddy viscosity model has a free constant that is calibrated by comparing with results from a second-order closure model. The new model is then used to calculate the variation of form drag on a stationary rigid wave with Reynolds number, R. The form drag increases by a factor of almost two as R drops from 2×10^4 to 2×10^3 and shows remarkably good agreement with the value measured by Zilker & Hanratty (1979). These calculations show that the damped eddy viscosity model captures the physical processes that produce the asymmetric pressure that leads to form drag and also wave growth.

Results from the numerical model show reasonable agreement with profiles measured over travelling water waves by Hsu & Hsu (1983), particularly for slower moving waves. The model suggests that the wave-induced flow in the water is irrotational except in an extremely thin interface layer, where viscous stresses are as likely to be important as turbulent stresses. Thus our study reinforces previous suggestions that the region very close to the interface is crucial to wind–wave interaction and shows that scales down to the viscous length may have an order-one effect on the development of the wave.

The energy budget and growth rate of the wave motions, including effects of the sheared current and Reynolds number, will be examined in a subsequent paper.

† Present address: Department of Mechanical Engineering, James Cook University, Townsville, Queensland 4811, Australia.
‡ Present address: Department of Meteorology, University of Reading, Reading RG6 2AU, UK.

1. Introduction

This paper is Part 2 of a series of three papers discussing the dynamics of the coupled turbulent air and water flows above and below water waves. Belcher, Harris & Street (1994, hereafter referred to as Part 1), developed an analytical model of the flow perturbations in the air and water caused by a moving water wave. As explained in Part 1, this analytical model is based on the approximation that the waves move slowly (as defined in Part 1). In this paper, Part 2, a numerical model is developed that is designed for slow, intermediate and fast moving waves and so allows solutions over the whole range of wind and wave speeds.

One motivation for continued study of wind–wave interactions is the scatter in the variation of wave growth rates with c/u_{*a} derived from field and laboratory experiments (c is the wave phase speed and u_{*a} is the air flow friction velocity). Is this scatter merely due to experimental variation and uncertainty, or can it be ascribed to variation of the growth rate with other parameters? There is a large body of theoretical evidence to suggest that there are several dimensionless parameters that have a primary influence on the wave growth rate. For example, many investigators (e.g. Miles 1957; Gent & Taylor 1976; Gent 1977; Riley, Donelan & Hui 1982; Al-Zanaidi & Hui 1984; Chalikov & Makin 1991; Belcher & Hunt 1993) have demonstrated a significant variation of wave growth rate with kz_0, where $k = 2\pi/\lambda$ is the wavenumber, λ is the wavelength, and z_0 is the interfacial roughness length.

Another parameter of potential importance to wave growth that has received little attention is the Reynolds number (e.g. based on the wavelength and friction velocity). Indeed, it is commonly assumed that air flow over ocean waves is aerodynamically rough and at high Reynolds number. It is of interest to examine the experimental field data of Snyder *et al.* (1981) to determine if this is actually the case. Assuming a logarithmic velocity profile in the air flow, the characteristic roughness length, z_0, and, hence, the roughness Reynolds number, $Re_r = z_0 u_{*a}/v_a$ (where v_a is the kinematic viscosity in the air), may be computed from the wind speed at a height of 5 m and friction velocity in the air tabulated in table 2 of Snyder *et al.* (1981). Out of 34 runs where it was possible to estimate the roughness Reynolds number in this manner, there are 6 smooth flow cases ($Re_r \leqslant 0.12$), 11 rough flow cases ($Re_r \geqslant 2.4$) and 17 transitional flow cases ($0.12 < Re_r < 2.4$). Additionally, assuming the deep-water dispersion relationship holds, the Reynolds number, defined by $R = u_{*a}\lambda/v_a$, was found to cover the range $66 \leqslant R \leqslant 9 \times 10^5$ (Harris 1992). Thus, the field data of Snyder *et al.* (1981) suggest the Reynolds number, R, is not necessarily large and the water surface is more likely to be aerodynamically transitional (or even smooth) than fully rough! The Reynolds number is usually considerably lower in laboratory wave facilities and low Reynolds number effects may be more pronouced. Hence, a careful examination of the effects of Reynolds number on the flow seems to be warranted.

Most previous models of wave growth have been uncoupled, i.e. they solve for the flow in the air only and apply boundary conditions at the air–water interface. It is usually assumed that the interfacial waves are irrotational, which thus ignores turbulent motions in the water. A more systematic approach is to solve simultaneously for the flow in the air and water and prescribe kinematic and dynamic coupling conditions at the interface. Such a coupled approach was used in Part 1 and is used here: it allows us to consider the effect of the turbulent motions in the water on the wave-induced flow field.

The numerical model presented here has two parts, the 'base flow model' and the 'perturbation flow model'. The base flow model calculates the coupled turbulent flow in the air and water with a flat interface and the perturbation flow model calculates linear perturbations to this base flow that are caused by a travelling wave of low slope. This same approach was used in the numerical models of flow over hills developed by Walmsley, Taylor & Keith (1986) and Beljaars, Walmsley & Taylor (1987). Here we exploit this linearized approach by using ideas for modelling the turbulent stress developed by Townsend (1980), Belcher, Newley & Hunt (1993), Belcher & Hunt (1993) and in Part 1. The main conclusion of their physical scaling arguments is that, although simple turbulence models based on local equilibrium between production and dissipation can be used to calculate the base flow, such an approach is neither appropriate nor accurate for the perturbed flow. Instead the perturbed flow has to be divided into inner and outer regions. In the inner region the wave-induced turbulence is in local equilibrium, and so it is appropriate to use an eddy viscosity model in this part of the flow. In the outer region, however, the turbulence is advected over the waves too rapidly to transport significant momentum and so an eddy viscosity model substantially overestimates the wave-induced stress. The wave-induced stress in the outer region can, however, be calculated using rapid distortion theory, which shows that the perturbation stress is much smaller than in the inner region. Hence the wave-induced stresses in the outer region are approximately zero. These ideas are important because the choice of model for the wave-induced Reynolds stress determines the accuracy of the pressure, and hence wave growth, calculations (e.g. Townsend 1972, 1980; Abrams & Hanratty 1985; Belcher & Hunt 1993; Harris & Street 1994). Second-order closure models (e.g. Launder, Reece & Rodi 1975) capture these effects, but are computationally expensive and not without their own problems. The linearized approach we use here of calculating the base and perturbation flows separately allows us to incorporate the ideas from the scaling and use different turbulence models for the base and perturbation flows, thus formulating a 'cheap' second-order closure.

Turbulent stresses in the base flow are approximated using the low-turbulence-Reynolds-number $k - \varepsilon$ model proposed by Launder & Sharma (1974), which can capture a whole turbulent boundary layer, including the viscous sublayer, and so is a generalization of the logarithmic profile specified in Part 1. This turbulence model is based on an eddy viscosity and was chosen here since Patel, Rodi & Scheuerer (1985) found that it was among the best of the near-wall turbulence models they evaluated in a variety of situations, including a boundary layer over a flat surface. This is encouraging because laboratory measurements made by Hsu, Hsu & Street (1981) and Cheung & Street (1988) show that the wave-averaged air flow over, and the wave-averaged water flow under, water waves closely resemble turbulent boundary layers over flat surfaces, which suggests that the Launder–Sharma turbulence model should produce reasonable profiles for the base flow.

For the wave-induced Reynolds stress we incorporate the conclusions from the scaling arguments described above and develop a *damped eddy viscosity model*, which is similar in philosophy to the truncated mixing length model used by Belcher *et al.* (1993), Belcher & Hunt (1993) and in Part 1. In the new method the wave-induced stress is modelled using an eddy viscosity, derived from the Launder–Sharma $k - \varepsilon$ model, that is multiplied by a damping function, which equals one in the inner region and decays to zero in the outer region. One aim of this paper is to explore the success of this method and the sensitivity to the damping function. This turbulence model

explicitly uses the results of linear analysis and its generalization to a nonlinear model may not be straightforward.

The remainder of the paper is organized as follows. The formulation of the model is outlined in §2 and an outline of the numerical solution is provided in §3. In §4, the model is tested by computing air flow over a sinusoidal hill and compared with Part 1 and Belcher *et al.* (1993). Next, the model is compared with the coupled analytical model of Part 1 for a slow wave. Finally, the model is used for flow in a laboratory wind-wave facility; the results are compared with the measurements of Hsu & Hsu (1983).

2. Formulation of the model equations

The air–water interface is dependent on time t' and is described by

$$\eta(x_1, t') = a \cos \left[k(x_1 - ct') \right], \tag{2.1}$$

where a is the wave amplitude. The right-handed coordinate system is arranged so that x_1 is in the streamwise direction (aligned with the wind), x_2 is in the vertical direction, and x_3 is in the horizontal direction normal to the wind. The Reynolds-averaged flow is considered to be two-dimensional in both the air and the water in the (x_1, x_2)-plane. The wave slope, ak, is restricted to be small (i.e. $\leqslant 0.1$).

Equations describing the base flow and perturbations to the base flow caused by the wave may be derived from the Navier–Stokes equations using a series of steps (e.g. see Norris & Reynolds 1975; Hsu *et al.* 1981; Al-Zanaidi & Hui 1984). The first step is to average the Navier–Stokes equations using the phase of the travelling surface wave as a reference. This phase-averaging process removes the turbulent velocity and pressure components but introduces unknown Reynolds stress terms which represent the effect of the turbulence on the phase-averaged flow. To provide closure it is necessary to introduce a model for the phase-averaged Reynolds stress; our choice is described in §§2.1 and 2.2. Next, all the equations are non-dimensionalized and transformed into a wavy coordinate system chosen so that the water surface becomes a coordinate line. The coordinate transformation is defined by

$$t' = t, \quad x_1 = x, \quad x_2 = z + f(z)\eta(x, t), \tag{2.2}$$

where $f(z)$ depends on the flow configuration (i.e. confined or unconfined) and is defined in §2.3. Following the transformation, the governing equations are expanded in powers of the wave slope, ak. For example, a flow quantity $q(x, z, t)$ is expanded as

$$q(x, z, t) = q_B(z) + \tfrac{1}{2}ak\{q_1(z)\exp[ik(x - ct)] + \text{complex conjugate}\}, \tag{2.3}$$

where q_B represents a base flow quantity and q_1 is the complex amplitude of the perturbation flow quantity. Note that the addition of the complex conjugate in the above definition ensures that the actual quantity $q(x, z, t)$ is purely real. Terms involving the same powers of the wave slope are collected into separate equations. Equations involving terms of zeroth-order in wave slope describe the base flow, whereas the equations that involve terms of first-order in wave slope describe linear perturbations to the base flow caused by the wave. Since the analysis is restricted to small wave slopes, terms of higher order in wave slope are neglected.

2.1. *Base flow*

The fully developed base flows in the air ($Z \geqslant 0$) and water ($Z \leqslant 0$) are governed by the phase-averaged momentum equations, with turbulence closure derived, as

explained in §1, from a low-turbulence-Reynolds-number $k - \varepsilon$ model (Launder & Sharma 1974). The resulting base flow equations are given in non-dimensional form by

X-momentum:

$$\frac{\partial}{\partial Z} \left[\left(\frac{\mathscr{V}}{R} + \bar{v}_{t_B} \right) \frac{\partial U_B}{\partial Z} \right] - \frac{1}{\mathscr{P}} \frac{\partial P_B}{\partial X} = 0, \tag{2.4}$$

K-equation:

$$\frac{\partial}{\partial Z} \left[\left(\frac{\mathscr{V}}{R} + \frac{\bar{v}_{t_B}}{\sigma_k} \right) \frac{\partial K_B}{\partial Z} \right] + \bar{v}_{t_B} \left(\frac{\partial U_B}{\partial Z} \right)^2 - \tilde{E}_B - D_B = 0, \tag{2.5}$$

$\tilde{E}$-equation:

$$\frac{\partial}{\partial Z} \left[\left(\frac{\mathscr{V}}{R} + \frac{\bar{v}_{t_B}}{\sigma_\varepsilon} \right) \frac{\partial \tilde{E}_B}{\partial Z} \right] + c_{1\varepsilon} f_1 \frac{\tilde{E}_B}{K_B} \bar{v}_{t_B} \left(\frac{\partial U_B}{\partial Z} \right)^2 - c_{2\varepsilon} f_2 \frac{\tilde{E}_B^2}{K_B} + G_B = 0, \tag{2.6}$$

where

$$\mathscr{V} = \begin{cases} v_w/v_a & \text{if } Z \leqslant 0 \\ 1 & \text{if } Z \geqslant 0 \end{cases}, \quad \mathscr{P} = \begin{cases} \rho_w/\rho_a & \text{if } Z \leqslant 0 \\ 1 & \text{if } Z \geqslant 0 \end{cases}, \tag{2.7}$$

$$D_B = \frac{2\mathscr{V}}{R} \left(\frac{\partial K_B^{1/2}}{\partial Z} \right)^2, \quad G_B = \frac{2\mathscr{V} \bar{v}_{t_B}}{R} \left(\frac{\partial^2 U_B}{\partial Z^2} \right)^2, \quad E_B = \tilde{E}_B + D_B. \tag{2.8}$$

The above equations have been made non-dimensional using a velocity scale u_{*_a}, a length scale $\mathscr{L}$, which is defined in §2.3, and a time scale $\mathscr{L}/u_{*_a}$. Subscripts a and w refer to the air and water, respectively. Additionally, where required in the non-dimensionalization, the fluid properties, such as density and viscosity, are defined to be those in the air. Hence, the dimensional values of velocity, pressure, turbulent kinetic energy, dissipation rate and eddy viscosity are given by $U_B u_{*_a}$, $P_B \rho_a u_{*_a}^2$, $K_B u_{*_a}^2$, $\tilde{E}_B u_{*_a}^3/\mathscr{L}$ and $\bar{v}_{t_B} u_{*_a} \mathscr{L}$, respectively. This non-dimensionalization leads to a Reynolds number defined by $R = u_{*_a} \mathscr{L}/v_a$.

In the Launder–Sharma model the eddy viscosity is

$$\bar{v}_{t_B} = c_\mu f_\mu K_B^2 / \tilde{E}_B, \tag{2.9}$$

where the functions f_1, f_2, f_μ and turbulence Reynolds number are defined by

$$f_1 = 1, \quad f_2 = 1 - 0.3 \exp\left(-R_T^2\right), \quad f_\mu = \exp\left[\frac{-3.4}{(1 + R_T/50)^2} \right], \quad R_T = \frac{R}{\mathscr{V}} \frac{K_B^2}{\tilde{E}_B}. \tag{2.10}$$

The function f_μ does not appear in the standard $k - \varepsilon$ model; Launder & Sharma (1974) introduced it to reduce the eddy viscosity in regions of low turbulence Reynolds numbers (e.g. near walls and the air–water interface). The values of the remaining constants are $c_\mu = 0.09$, $c_{1\varepsilon} = 1.44$, $c_{2\varepsilon} = 1.92$, $\sigma_k = 1.0$, and $\sigma_\varepsilon = 1.3$, which are the same as for the standard high-Reynolds-number $k - \varepsilon$ turbulence model (we have not tuned this model in any way and all values of the constants are standard). For high turbulence Reynolds numbers, R_T, the functions f_μ and f_2 tend to unity, and the Launder–Sharma model reduces to the standard $k - \varepsilon$ model.

The equations governing the base flow comprise a coupled sixth-order set of nonlinear ordinary differential equations. The order of the governing equations may be reduced by one since it is possible to integrate equation (2.4) for fully developed

flow (i.e. constant $\partial P_B/\partial X$) to yield

$$\bar{\tau}_B(Z) = \mathscr{P}\left(\frac{\mathscr{V}}{R} + \bar{v}_{t_B}\right)\frac{\partial U_B}{\partial Z} = \frac{\partial P_B}{\partial X}Z + 1, \tag{2.11}$$

where $\bar{\tau}_B(Z)$ is the dimensionless base flow shear stress and continuity of base flow shear stress across the interface has been used (see Appendix B).

2.2. *Perturbed flow*

The equations of first-order in wave slope that govern perturbations to the base flow are presented below in non-dimensional form:
continuity:

$$i\mathscr{K}U_1 + V_1' - ifU_B' = 0, \tag{2.12}$$

X-momentum:

$$-i\mathscr{K}CU_1 + iCfU_B' + U_B(i\mathscr{K}U_1 - ifU_B') + V_1U_B'$$
$$= -\frac{i\mathscr{K}P_1}{\mathscr{P}} + \left(\frac{\mathscr{V}}{R} + \bar{v}_{t_P}\right)\left(-i\mathscr{K}V_1' + U_1'' - \frac{2f'U_B''}{\mathscr{K}} - \frac{f''U_B'}{\mathscr{K}}\right)$$
$$+ \bar{v}_{t_P}'\left(\frac{-2f'U_B'}{\mathscr{K}} + i\mathscr{K}V_1 + U_1'\right) + \bar{v}_{t_1}U_B'' + \bar{v}_{t_1}'U_B', \tag{2.13}$$

Z-momentum:

$$-i\mathscr{K}CV_1 + i\mathscr{K}U_BV_1 = -\frac{P_1'}{\mathscr{P}} + \left(\frac{\mathscr{V}}{R} + \bar{v}_{t_P}\right)(-\mathscr{K}^2V_1 + V_1'') + \bar{v}_{t_P}'(-ifU_B' + 2V_1') + i\mathscr{K}\bar{v}_{t_1}U_B', \tag{2.14}$$

K-equation:

$$-iC\mathscr{K}K_1 + iCfK_B' + i\mathscr{K}K_1U_B + V_1K_B' - ifU_BK_B'$$
$$= \left(\frac{\mathscr{V}}{R} + \frac{\bar{v}_{t_P}}{\sigma_k}\right)\left(-\mathscr{K}^2K_1 + \mathscr{K}fK_B' - \frac{f''K_1'}{\mathscr{K}} + \frac{2f'K_B''}{\mathscr{K}} + K_1''\right)$$
$$+ \frac{\bar{v}_{t_P}'}{\sigma_k}\left(\frac{2f'K_B'}{\mathscr{K}} + K_1'\right) + \frac{\bar{v}_{t_1}K_B''}{\sigma_k} + \frac{\bar{v}_{t_1}'K_B'}{\sigma_k}$$
$$+ \bar{v}_{t_P}\left(2i\mathscr{K}V_1U_B' + \frac{2f'U_B'^2}{\mathscr{K}} + 2U_B'U_1'\right) + \bar{v}_{t_1}U_B'^2 - \tilde{E}_1 - D_1, \tag{2.15}$$

$\tilde{E}$-equation:

$$-iC\mathscr{K}\tilde{E}_1 + iCf\tilde{E}_B' + i\mathscr{K}\tilde{E}_1U_B + V_1\tilde{E}_B' - ifU_B\tilde{E}_B'$$
$$= \left(\frac{\mathscr{V}}{R} + \frac{\bar{v}_{t_P}}{\sigma_\varepsilon}\right)\left(-\mathscr{K}^2\tilde{E}_1 + \mathscr{K}f\tilde{E}_B' - \frac{f''\tilde{E}_1'}{\mathscr{K}} + \frac{2f'\tilde{E}_B''}{\mathscr{K}} + \tilde{E}_1''\right)$$
$$+ \frac{\bar{v}_{t_P}'}{\sigma_\varepsilon}\left(\frac{2f'\tilde{E}_B'}{\mathscr{K}} + \tilde{E}_1'\right) + \frac{\bar{v}_{t_1}\tilde{E}_B''}{\sigma_\varepsilon} + \frac{\bar{v}_{t_1}'\tilde{E}_B'}{\sigma_\varepsilon}$$
$$+ c_{1\varepsilon}f_1\bar{v}_{t_P}\left(\frac{2i\mathscr{K}V_1U_B'\tilde{E}_B}{K_B} + \frac{2f'U_B'^2\tilde{E}_B}{\mathscr{K}K_B} + \frac{2U_B'U_1'\tilde{E}_B}{K_B} + \frac{U_B'^2\tilde{E}_1}{K_B} - \frac{U_B'^2\tilde{E}_BK_1}{K_B^2}\right)$$
$$+ c_{1\varepsilon}f_1\bar{v}_{t_1}\frac{\tilde{E}_B}{K_B}U_B'^2 - c_{2\varepsilon}f_2\left(\frac{2\tilde{E}_B\tilde{E}_1}{K_B} - \frac{\tilde{E}_B^2K_1}{K_B^2}\right) + G_1, \tag{2.16}$$

where

$$D_1 = \frac{\mathscr{V}}{R} \left(-\frac{f' K_B'^2}{\mathscr{K} K_B} - \frac{K_1 K_B'^2}{2 K_B^2} + \frac{K_B' K_1'}{K_B} \right), \tag{2.17}$$

$$G_1 = \frac{2\mathscr{V} \bar{v}_{t_P}}{R} \left(-\frac{2 f'' U_B' U_B''}{\mathscr{K}} + \frac{4 f' U_B''^2}{\mathscr{K}} + 2 U_B''^2 U_1'' \right) + \frac{2\mathscr{V} \bar{v}_{t_1} U_B''^2}{R}, \tag{2.18}$$

and the primes denote differentiation with respect to Z. The non-dimensional wavenumber and wavespeed are defined by $\mathscr{K} = 2\pi \mathscr{L}/\lambda$ and $C = c/u_{*_a}$, respectively. Equations (2.12)–(2.18) comprise a ninth-order set of coupled ordinary differential equations and are linear in the perturbation quantities (U_1, V_1, P_1, K_1, and $\tilde{E}_1$), since the base flow profiles $U_B(Z)$, $K_B(Z)$, and $\tilde{E}_B(Z)$ and their corresponding derivatives are known from solution of the base flow equations. The perturbation pressure in the above equations represents the deviation from hydrostatic pressure relative to the mean water level (i.e. $x_2 = 0$).

2.2.1. *Damping the eddy viscosity*

As explained in §1, the wave-induced Reynolds stress is modelled here using a new and computationally inexpensive model, the *damped eddy viscosity model*. Accordingly, the eddy viscosity derived from the Launder–Sharma $k - \varepsilon$ model is multiplied by a damping function, f_d, which must equal one in the inner-region and must tend to zero in the outer region. Thus the eddy viscosity for the perturbed flow is

$$\bar{v}_{t_P} = f_d \bar{v}_{t_B} = c_\mu f_p K_B^2 / \tilde{E}_B, \tag{2.19}$$

where $\bar{v}_{t_B}$ is the usual eddy viscosity derived from the $k - \varepsilon$ model and $f_p = f_\mu f_d$. The damping function is chosen to be an exponential that must decay upwards on a distance that scales with the inner-region scale, hence

$$f_d = \begin{cases} 1 & \text{if } |Z| < Z_l \\ \exp(1 - |Z|/Z_l) & \text{if } |Z| \geqslant Z_l, \end{cases} \tag{2.20}$$

where $Z_l = \alpha_d l/\mathscr{L}$, where l is the inner-region length scale defined in Part 1 by (4.3) for the air flow and by (4.5) for the water flow. Note that here the model is making explicit use of results from linear theory, namely the definition of l. The coefficient α_d is a model constant, whose value will be determined in §4 by comparing results for the perturbation shear stress with results from a second-order closure model. The form of this damping function is empirical and its value will be assessed by comparing with data in §4.

Equations (2.12)–(2.18) also contain a perturbation eddy viscosity, $\bar{v}_{t_1}$, that represents the influence of the wave on the turbulence structure (to order ak). The relationship between $\bar{v}_{t_1}$ and the perturbation quantities K_1 and $\tilde{E}_1$ results from an expansion of the original eddy viscosity definition and is given by

$$\bar{v}_{t_1} = \left(2 c_\mu f_p K_B / \tilde{E}_B \right) K_1 - \left(c_\mu f_p K_B^2 / \tilde{E}_B^2 \right) \tilde{E}_1. \tag{2.21}$$

Notice how this perturbation eddy viscosity is also damped through its dependence on f_p. Expressions for the derivatives of $\bar{v}_{t_P}$, $\bar{v}_{t_1}$, f_p and f_μ are required and were obtained by differentiation of the appropriate definitions.

The base flow and perturbed flow Reynolds stresses may be expressed in terms of the eddy viscosity and other flow quantities using the expansion procedure (Harris 1992). For example, the base flow shear stress is defined by $(r_{12})_B = -\bar{v}_{t_B} U_B'$ while the

Case	$\mathscr{L}$	$\mathscr{K}$	$f(Z)$
Confined uncoupled (CU)	H	variable	$\dfrac{\sinh(\mathscr{K} - \mathscr{K}Z)}{\sinh \mathscr{K}}$ for $0 \leqslant Z \leqslant 1$
Confined coupled (CC)	$2H$	variable	$\dfrac{\sinh(\mathscr{K}/2 + \mathscr{K}Z)}{\sinh(\mathscr{K}/2)}$ if $-\frac{1}{2} \leqslant Z \leqslant 0$ $\dfrac{\sinh(\mathscr{K}/2 - \mathscr{K}Z)}{\sinh(\mathscr{K}/2)}$ if $0 \leqslant Z \leqslant \frac{1}{2}$
Unconfined uncoupled (UU)	λ	2π	$\exp(-\mathscr{K}Z)$ for $0 \leqslant Z \leqslant 1$
Unconfined coupled (UC)	2λ	4π	$\exp(\mathscr{K}Z)$ if $-\frac{1}{2} \leqslant Z \leqslant 0$ $\exp(-\mathscr{K}Z)$ if $0 \leqslant Z \leqslant \frac{1}{2}$

TABLE 1. Definition of length scales and coordinate transform functions for each flow configuration.

perturbation shear stress is given by

$$(r_{12})_1 = -\mathrm{i}\mathscr{K} V_1 \bar{v}_{t_P} - \bar{v}_{t_P} U_1' - \bar{v}_{t_1} U_B' + f' \bar{v}_{t_P} U_B'/\mathscr{K}. \tag{2.22}$$

2.3. Flow configurations

The numerical model can treat two flow configurations: *confined* flow, when walls are located a distance H above and below the interface (figure 1*a*); and *unconfined* flow, when there are no confining walls such as in the ocean (figure 1*b*). When the geometry is confined the flow is forced by a pressure gradient in the air, whereas when the geometry is unconfined the flow is forced by specifying that the air flow relaxes to a constant stress layer far above the wave (see Appendix A). Each configuration may be solved in the air only using prescribed boundary conditions at the interface (*uncoupled* flow), or solved simultaneously in both the air and water using coupling conditions at the interface (*coupled* flow). This yields four possible model types. For convenience, each model type uses a different length scale, $\mathscr{L}$, to non-dimensionalize the governing equations. The model configuration and type determines the length scales and transform function, which are summarized in table 1. For the particular coupled confined case studied in §4, the water and air occupy equal heights (H) in the channel and the length scale is chosen as the overall channel height, $2H$. Boundary and coupling conditions used for each configuration are presented Appendices A and B, respectively.

3. Numerical solution

3.1. Base flow equations

For all the flow configurations the base flow governing equations reduce to fifth-order sets of nonlinear ordinary differential equations. Along with their boundary and coupling conditions, they comprise either two- or three-point boundary value problems (BVPs), depending on whether the configuration is coupled flow or uncoupled flow. Defining $A_B = (\mathscr{V}/R + \bar{v}_{t_B}/\sigma_k)K_B'$ and $B_B = (\mathscr{V}/R + \bar{v}_{t_B}/\sigma_\varepsilon)\tilde{E}_B'$, the BVP may be expressed as a set of first-order ODEs given by

$$y' = f(Z, y), \quad \text{where } y = \left\{U_B, K_B, \tilde{E}_B, A_B, B_B\right\}^T, \tag{3.1}$$

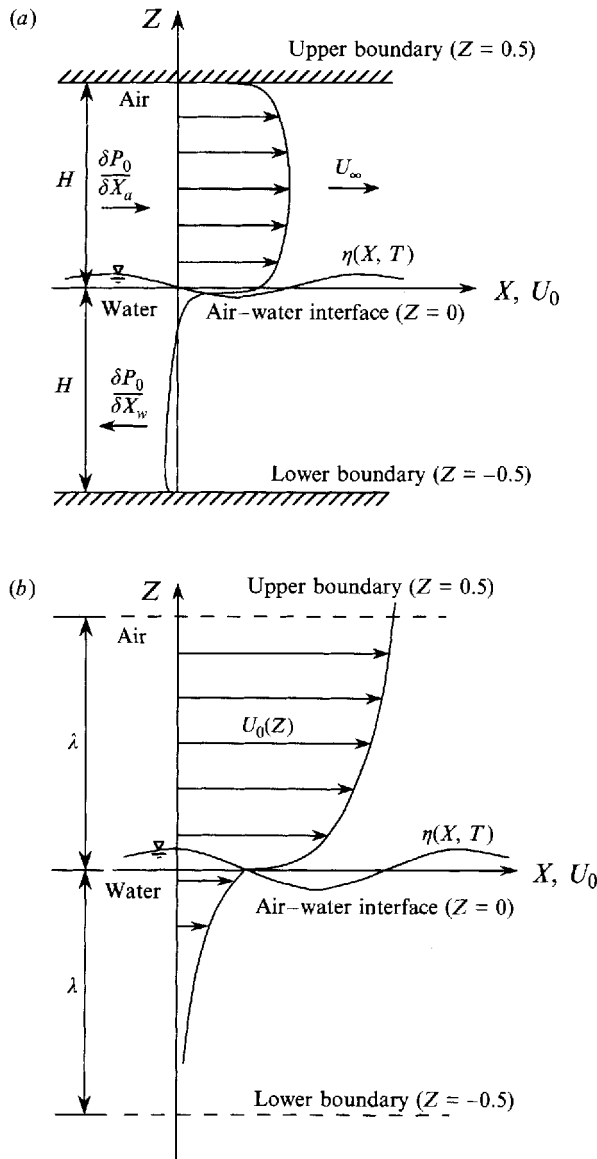FIGURE 1. Flow configurations of the numerical model:
(*a*) confined coupled; (*b*) unconfined coupled.

and f may be assembled from the base-flow equations in §2.1 (see Harris 1992 and Harris & Street 1994). Equation (3.1) was solved using the finite difference method with Newton iteration for nonlinear BVPs described by Ascher, Mattheij & Russel (1988). The derivative term was represented using the one-step, second-order accurate midpoint method. This method avoids the singularity in the $k - \varepsilon$ equations at the boundaries, and also guarantees second-order accuracy for non-uniform grid spacings. After application of Newton's method to the discretized form of equation (3.1), the resulting algebraic expressions were assembled into a banded block matrix. In the coupled problems, the coupling conditions were expressed in matrix form and included into the banded matrix. Given a suitable initial guess, this method gives quadratic

convergence to the solution and the base-flow problems typically converge in less than ten iterations.

The confined flow configurations involve auxiliary conditions which must be satisfied by adjusting the pressure gradient(s). In such cases an iterative procedure is used in which the pressure gradients are adjusted based on the present solution (using an extrapolation method) and the problem re-solved until the auxiliary condition is satisfied.

The solution of equation (3.1) for y yields profiles of U_0, K_0, $\tilde{E}_0$, A_0 and B_0, as well as profiles of the gradients U_0', K_0', and $\tilde{E}_0'$. These gradient profiles are numerically differentiated using a cubic spline technique to yield the second derivatives required for input to the perturbed flow equations.

Complete details of the solution of the base flow equations, including details of the finite difference method, generation of the Jacobian matrix needed for Newton's method, assembly of the coupling and boundary conditions, and overall solution algorithm may be found in Harris (1992).

3.2. *Perturbed flow equations*

Although the equations governing the perturbed flow are linear, they are challenging to solve since the solution gradients are very steep near the interface and confining walls (if present). The governing equations may be written in the form

$$y' = Ay + q, \quad \text{where } y = \left\{ U_1, U_1', V_1, V_1', P_1, K_1, K_1', \tilde{E}_1, \tilde{E}_1' \right\}^T, \qquad (3.2)$$

A is the coefficient matrix and q is the inhomogeneous vector. Assembly of the equations into the above form requires several steps, as detailed in Harris (1992).

The fourth-order-accurate, implicit two-stage Gauss method for linear problems described in Ascher *et al.* (1988) was used to solve equation (3.2). This scheme has similar advantages to the midpoint scheme used for the solution of the base flow equations.

The continuity equation is not solved explicitly in the above formulation (instead, its derivative is used), and so terms in the continuity equation (2.12) were evaluated separately at each value of Z and combined together to provide a convenient method of checking the accuracy of the numerical solution. It was found that a relative error (the maximum error in the continuity equation divided by the magnitude of the maximum term) of less than about 10^{-5} was reached when the solution was grid-independent. For the cases presented in this paper, up to 800 grid points were used for the uncoupled cases and up to 1600 grid points were required in the coupled cases (800 each in the air and water). Non-uniform meshes were used in which the grid points were closely spaced near the solid boundaries (in the confined flow cases) and each side of the air–water interface, and distributed logarithmically away from the boundaries (or interface). The Reynolds number was used as a parameter to determine the grid spacing (for higher Reynolds numbers the grid was more closely spaced near the wall(s) and the interface). In all simulations the base flow model and the perturbation model were solved on the same grid which helped avoid the possibility of interpolation errors when the base flow profiles were input to the perturbation model. Further details are given in Harris (1992).

For calculations of the coupled perturbation flow cases the complex wave speed C is an unknown eigenvalue and must be chosen to satisfy the kinematic boundary condition (see Appendix B). An iterative procedure was used in which the wave speed was initially guessed, the coupled perturbation problem solved and the kinematic bound-

ary condition checked and used to adjust the wave speed after each iteration. Note that the Froude number (defined in Appendix B) is held constant during this iteration process. Using the wave speed computed from the deep-water dispersion relationship as an initial guess, convergence was typically achieved in about 5 iterations.

4. Results and discussion

We now present a sequence of results from the numerical model together with comparisons with other studies. First, the model is run for flow over a stationary rigid wave (a hill) in order to calibrate the new damped eddy viscosity model (i.e. to set the value of the parameter α_d) and to evaluate the success of the damped model compared with the undamped model. Secondly, the model is compared with the coupled analytical model presented in Part 1. Finally, the model is compared in detail with the experimental measurements of flow over water waves performed by Hsu *et al.* (1981) and Hsu & Hsu (1983).

4.1. *Unconfined flow*

In unconfined flow the parameter $\mathcal{K}$ is constant, but the numerical model of the base flow retains two parameters, namely the Reynolds number, R, which characterizes the viscous stress, and the roughness Reynolds number, Re_r, which characterizes the interface. In the analytical model of Part 1, the base flow is parameterized solely by the interfacial roughness length, z_0, which characterizes either the height of the roughness elements (the ripples) or the depth of the viscous sublayer, when $z_0 = 0.11\nu_a/u_{*a}$. Solutions were constructed in Part 1 on the assumption that $1/\ln(1/kz_0) \ll 1$, so that the roughness elements, or viscous sublayer, are much thinner than the inner-region. Thus for comparison with the analytical model for given kz_0 the two parameters of the numerical model must be chosen such that

$$kz_0 = \mathcal{K} Re_r/R, \tag{4.1}$$

and R must be sufficiently large that the viscous sublayer is much thinner than the inner region (i.e. $Z_a^+ \gg 20$); then the viscous stresses are negligible in the bulk of the inner region as assumed in the analytical model.

It is of interest to focus on smooth flow and compare the depth of the viscous sublayer with the depth of the inner region. We can then determine how large the Reynolds number should be to meaningfully neglect viscous stresses. From equation (4.3) of Part 1, the dimensionless depth of the inner region in the air, $Z_a = l_a/\mathscr{L}$, is defined implicitly by

$$\mathcal{K} Z_a[\ln(Z_a R/Re_r) - \kappa C] = 2\kappa^2. \tag{4.2}$$

Consider a stationary wave ($C = 0$), which produces the smallest value of Z_a (see figure 4 in Part 1). For the uncoupled unconfined case ($\mathcal{K} = 2\pi$) and smooth flow ($Re_r = 0.11$), the above equation yields $Z_a = 8.54 \times 10^{-3}$ for $R = 5 \times 10^3$ and $Z_a = 5.93 \times 10^{-3}$ for $R = 10^5$. In law-of-the-wall coordinates, these values correspond to $Z_a^+ = Z_a R = 43$ for $R = 5 \times 10^3$ and $Z_a^+ = 590$ for $R = 10^5$. Thus, for the lower Reynolds number, the viscous sublayer (which has a depth of about $z^+ = 20$) is almost half the inner-region depth and so cannot meaningfully be neglected. In contrast, for the higher Reynolds number example, the depth of the viscous region is only a small fraction of the inner-region depth and so may be neglected (as in the analytical model of Part 1). These two Reynolds numbers lie well within the range

of Reynolds numbers likely for ocean waves (see §1), and so molecular viscosity can play a role in wave growth, even in flow over the ocean.

A similar argument also applies in the water; the difference is that the depth of the inner region is so small that molecular viscosity is almost always important (except possibly around $C \approx 0$).

4.1.1. *Shear stress profile over a stationary rigid wave*

In Part 1 it was shown that the imaginary part of the perturbation pressure at the interface, which is responsible for the bulk of the wave growth under most conditions, can be related to the real part of the perturbation shear stress profile (i.e. the part that gives the profile of the shear stress perturbation over the wave crest). So we now compare the perturbation shear stress profiles from the numerical model, calculated for a stationary rigid wavy wall ($C = 0$ and $U_1 = V_1 = 0$ on the wall), with profiles calculated analytically by Belcher *et al.* (1993) and profiles computed by Newley (1986) using a nonlinear numerical model with the second-order Reynolds stress closure model of Launder *et al.* (1975) (see Belcher *et al.* figure 7). These comparisons will be used to select an appropriate value for the damping coefficient α_d (defined in (2.20)). In the present notation the parameters used by Belcher *et al.* are $ak = \pi/50$ and $z_0/\lambda = 10^{-4}$. The parameters of the present numerical model were selected to be $Re_r = 10$ (fully rough flow) and $R = 10^5$, giving $z_0/\lambda = 10^{-4}$, $Z_a = 1.09 \times 10^{-2}$ and $Z_a^+ = 1086 \gg 20$, as required. In this case the actual combination of Re_r and R chosen makes little difference. In the notation of the present model, the total shear stress perturbation, $\Delta\tau$, is given by

$$\Delta\tau = ak[(r_{12})_1 + (\tau_{12})_1], \tag{4.3}$$

where $(r_{12})_1$ is defined by equation (2.22) and $(\tau_{12})_1 = (1/R + \bar{v}_{t_P})(\mathrm{i}\mathscr{K} V_1 + U_1' - f'U_0'/\mathscr{K}) + \bar{v}_{t_1} U_0'$ is the perturbation to the viscous shear stress, which is included in this comparison only for completeness; in this rough flow case, the viscous shear stress is much smaller than the Reynolds stress except *very* near surface.

Profiles from the present model of the real and imaginary components of the shear stress perturbation above a sinusoidal hill are shown in figures 2(*a*) and 2(*b*) respectively. In each figure there are three curves: one corresponds to the undamped eddy viscosity model, and the other two correspond to the damped eddy viscosity model with $\alpha_d = 1.0$ and 2.0. Figure 2(*a*) shows that the undamped eddy viscosity model predicts large values of the real part of the perturbation shear stress in the outer region, whereas the new damped eddy viscosity model gives perturbation shear stresses that decay quickly in the outer region. The choice of the constant α_d clearly has an effect on profiles of the shear stress. The choice $\alpha_d = 1.0$ severely damps the negative peak in the real part of the shear stress (figure 2*a*) and the positive peak in the imaginary part of the shear stress (figure 2*b*) and we interpret this value of α_d to be too low. However, a value of $\alpha_d = 2.0$ is better as it leaves the negative peak in the real part of the shear stress intact, while still effectively damping the eddy viscosity in the outer region.

Figure 3 shows a comparison of the computed shear stress profiles with the results of the numerical model of Newley (1986) and the analytical model of Belcher *et al.* (1993). The comparison is given only near the interface and, for consistency with previously published results, the distance from the interface is expressed as z/l_a, where l_a is the inner-region length scale as defined by Belcher *et al.* (1993). Note that their definition yields $Z_a = l_a/\lambda = 1.58 \times 10^{-2}$ rather than the present definition (see Part 1) which gives $Z_a = 1.09 \times 10^{-2}$. There are two curves corresponding to
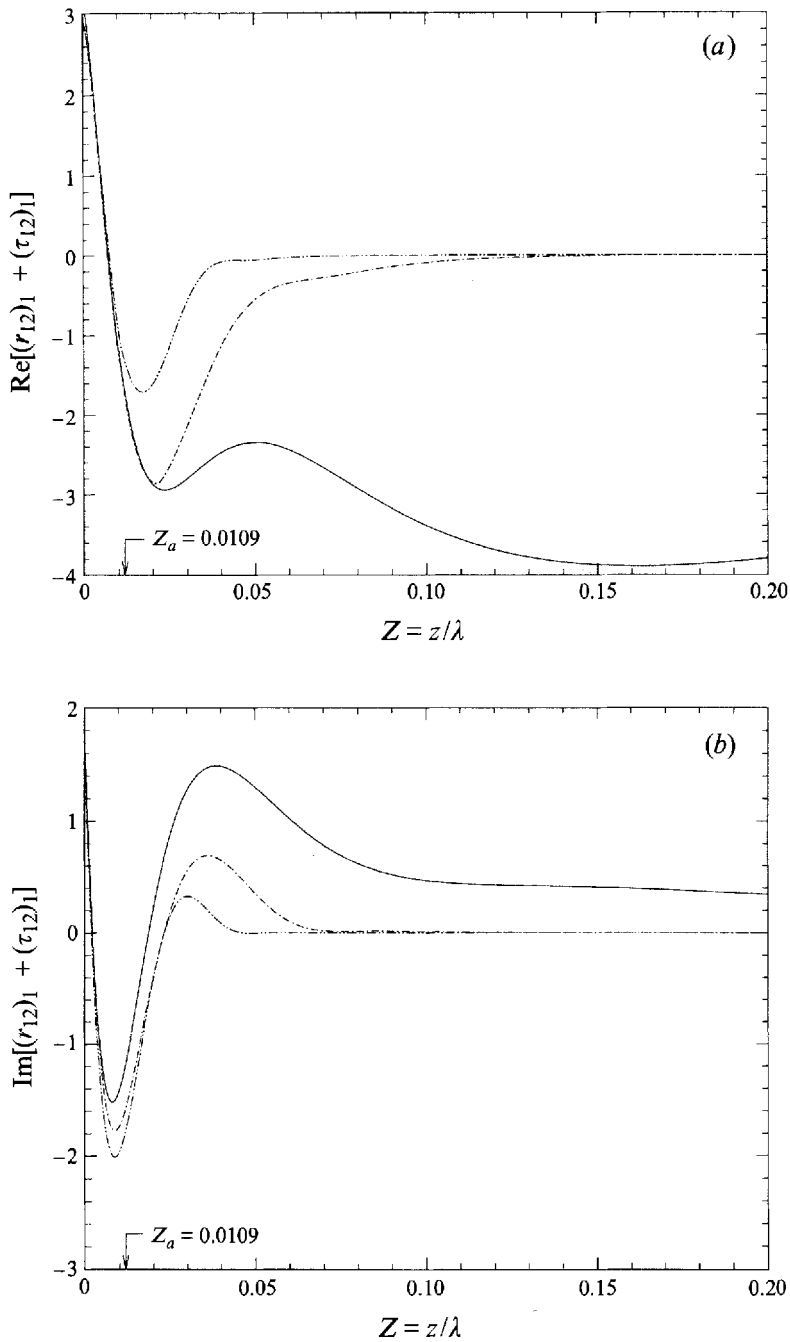
FIGURE 2. Effect of damping coefficient α_d on the perturbation shear stress profile above a sinusoidal hill: (a) at the crest; (b) at the upwind slope. ——, Undamped model; —·—, damped model, $\alpha_d = 2$; ····, damped model, $\alpha_d = 1$.

the Newley model since it is nonlinear and so gives different profiles at the crest and trough (figure 3a) and at the upwind and downwind slopes (figure 3b). The profiles at the trough and downwind slope in figures 3(a) and 3(b), respectively, have had their signs reversed for comparison purposes. The difference between the profiles at the crest and trough or at the upwind and downwind slope then provides a measure of nonlinear effects.

Figure 3(a) shows that the real part of the perturbation shear stress predicted by the undamped numerical model is in good agreement with the Newley model for $z/l_a \lesssim 1$. However, as noted above, the undamped model drastically overpredicts the perturbation shear stress for $z/l_a \gtrsim 2$ (i.e. in the outer region) since the equilibrium turbulence model is inappropriate. The proposed damped eddy viscosity model, with $\alpha_d = 2.0$, shows remarkably good agreement with the much more sophisticated (and computationally expensive) second-order Reynolds stress model used in Newley's model. Notice that damping the eddy viscosity makes virtually no difference to the values of the shear stress perturbation at the wavy surface (in agreement with the analysis of Belcher *et al.* 1993) and both the damped and undamped models are in excellent agreement with the second-order closure model very near the surface. The analytical model of Belcher *et al.* (1993) also shows good agreement with the real part of the perturbation shear stress. The profile from the theory is truncated at $Z = l_a$ for reasons explained in Belcher *et al.* (1993).

Figure 3(b) shows the imaginary part of the perturbation shear stress predicted by the present numerical model, which shows reasonable agreement with the second-order closure model predictions. Unfortunately, damping the eddy viscosity actually worsens the agreement between the present model and the second-order closure model in the outer region. The profiles of $\mathrm{Im}(\Delta\tau)$ predicted by the analytical theory of Belcher *et al.* (1993) show poor agreement with the second-order closure model in the near surface region. The nonlinear effects are more pronounced on the wave slopes (i.e. for $\mathrm{Im}(\Delta\tau)$) where there is about a 30% difference between the maximum negative values (at $z/l_a \approx 0.45$). Indeed, at the sloping part of the wave the boundary layer experiences either an accelerating or a decelerating pressure gradient and the rapid distortion effects might be expected to operate right down to the surface (Belcher *et al.* 1993). Thus, the shear stress profiles at the upwind and downwind wave slopes are more difficult to model accurately than those at the wave crest or trough. Perhaps a more sophisticated damping function is needed to model this part of the flow. Fortunately, the growth rate of the wave is related to the real part of the perturbation shear stress so that this discrepancy does not affect the ability of the models to predict realistic wave growth rates.

4.1.2. *Form drag on a stationary rigid wave*

The growth rate of the wave is related to the form drag on the wave, and there has been much recent interest in calculating the form drag on a stationary rigid wave, i.e. a hill (e.g. Belcher *et al.* 1993; Wood & Mason 1993; Xu & Taylor 1995). Belcher *et al.* (1993) show that using the mixing-length model throughout the flow results in form drag predictions that are too large by a factor of about two (depending on the value of kz_0). The uncoupled unconfined version of the present numerical model was used to compute the form drag on a sinusoidal hill for comparison with previous results. For these runs combinations of R and Re_r were selected to give fully rough flow ($Re_r > 2.4$) and $Z_a^+ \gg 20$ over a range of values of kz_0. The model was run with no damping (i.e. the isotropic eddy viscosity model over the full domain) and with
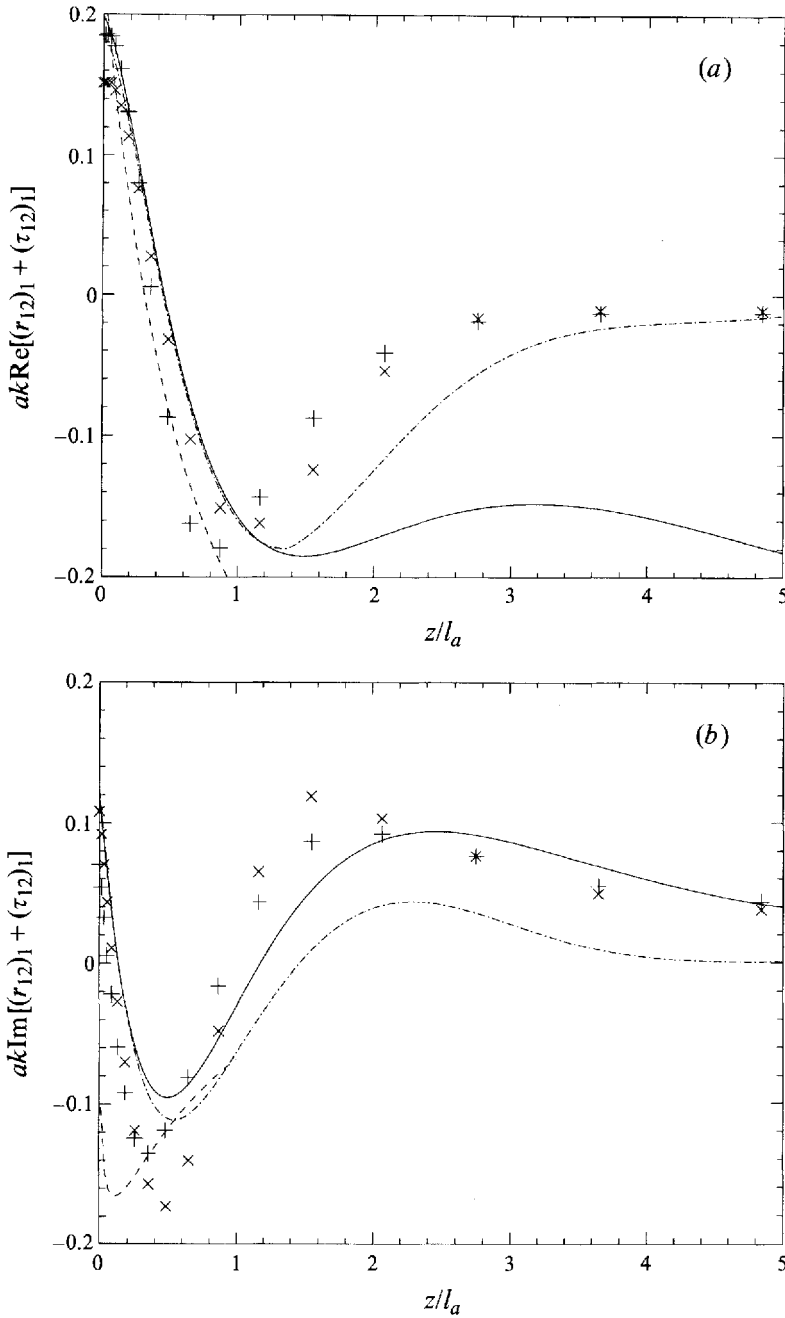
FIGURE 3. Perturbation shear stress profile above a sinusoidal hill: (*a*) at the crest; (*b*) at the upwind slope. ——, Undamped model; —·—, damped model, $\alpha_d = 2$; - - -, theory with truncated mixing length (Belcher *et al.* 1993) ; ×, numerical model with second-order closure (Newley 1986) (*a*) at crest (*b*) at upwind slope; +, numerical model with second-order closure (Newley 1986) (*a*) at trough (*b*) at downwind slope (see text).

damping, using $\alpha_d = 0.5$, 1 and 2. In each case the imaginary part of the perturbation pressure at the surface was computed and used to evaluate the dimensionless form drag perturbation (per unit width in the x_3 direction) on the hill, which is given by

$$\Delta F/(\rho_a u_{*_a}^2 a^2 k) = \pi \text{Im}(P_1). \qquad (4.4)$$

The values of R, Re_r and the resulting form drag computed by our model are summarized in table 2. The values of Z_a^+ range from 168 for the lowest Reynolds number to 10150 for the highest Reynolds number, so that the condition $Z_a^+ \gg 20$ is satisfied in all cases. Table 2 shows that the values of the form drag are dependent to some extent on α_d. As α_d decreases from ∞ (no damping) to $O(1)$ the form drag also decreases, but for $\alpha_d \leqslant 1$ the drag coefficient is approximately constant; in fact, the computed drag coefficients are almost identical for $\alpha_d = 0.5$ and $\alpha_d = 1$. However, as demonstrated in §4.1.1 above, $\alpha_d = 2$ appears to give the best profiles of shear stress.

The computed drag coefficients are plotted as a function of the normalized roughness length, kz_0, in figure 4, along with the data presented in Part 1, figure 11. The results from the undamped model are similar to, but somewhat lower than, the theoretical and numerical results obtained using mixing-length throughout the flow (see Part 1). These curves all considerably overestimate the form drag. But the damped eddy viscosity model, with $\alpha_d = 1$ and 2, yields essentially identical results to the numerical model of Newley (1986), which incorporates second-order closure; and is consistent with the truncated mixing-length analytical model of Belcher *et al.* (1993) for values of $1/\ln(1/kz_0) \lesssim 0.14$. The form drag calculated with the analytical model deviates from the present computations and the results of Newley (1986) for $1/\ln(1/kz_0) \gtrsim 0.14$ since the thickness of the inner region then becomes large and so one of the assumptions of the analysis ceases to be valid. For instance, when $1/\ln(1/kz_0) = 0.15$, $kl_a/(2\kappa^2) = 0.243$ (from equation (4.3) in Part 1) which is no longer small compared with unity.

Ideally, the numerical model predictions would extend to lower values of kz_0; however, while this is possible, to do so requires very high Reynolds numbers and a very large number of grid points for grid-independence. On the other hand, the analytical model is ideally suited to low values of kz_0 and so the theory and numerics are complementary in this respect.

In Part 1, figure 11 showed a value of the form drag measured by Zilker & Hanratty (1979). Unfortunately, this value was incorrectly plotted (we are indebted to Kees Mastenbroek for pointing out this error). This error has prompted us to look more carefully at these data and at the effect of Reynolds number on form drag. Zilker & Hanratty (1979) report values of $\frac{1}{2}U_b H/v_a$ and kv_a/u_* which imply $U_b/u_* = 19.8$ and hence the Reynolds number of their experiment is $R = 2960$. In addition they report smooth flow ($Re_r = 0.11$), $\mathcal{K} = kH = 2\pi$, $ak = 0.157$ and $C = 0$. They also measured the surface pressure perturbation and calculated a drag coefficient: $C_D = \Delta F/(\frac{1}{2}\rho U_b^2 \lambda) = 1.26 \times 10^{-3}$, which implies $\Delta F/(\rho_a u_*^2 a^2 k) = 62.8$ (using $U_b/u_* = 19.8$). This value of the drag coefficient is plotted in figure 5, which shows the variation of drag coefficient with Reynolds number, R, for smooth flow ($Re_r = 0.11$). Also shown on figure 5 are the drag coefficients obtained from the confined uncoupled version of the numerical model (using both damped and undamped closures) and results from the theoretical model with $z_0 = 0.11v/u_*$.

At high Reynolds numbers ($R \gtrsim 2 \times 10^4$) the damped numerical model agrees well with the theoretical model, but as R decreases the numerical model shows a striking increase compared with the theory. Presumably this increase is because viscous stresses
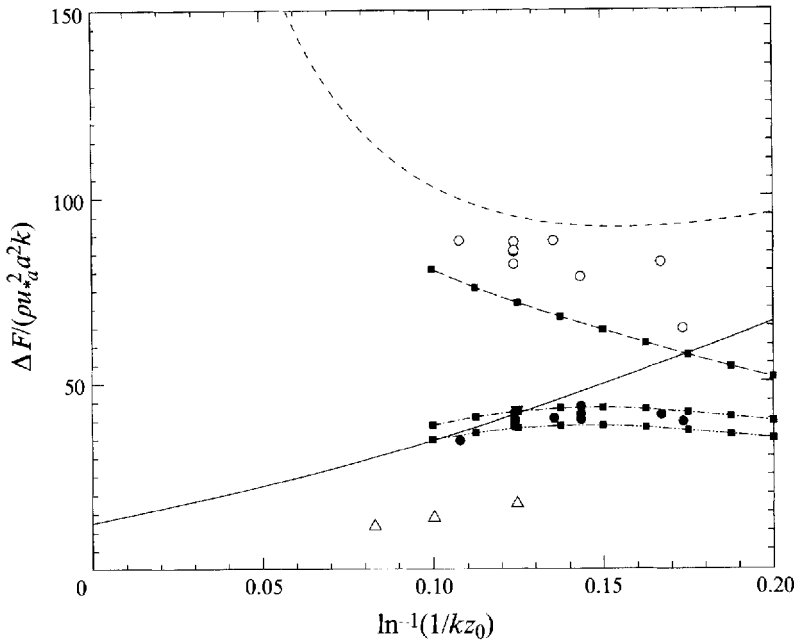
FIGURE 4. Drag coefficient on a sinusoidal hill: – ■ –, undamped model; —·–■–·—, damped model, $\alpha_d = 2$; ···–■–···, damped model, $\alpha_d = 1$; ——, theory with truncated mixing length (Belcher *et al.* 1993); - - -, theory with mixing length throughout flow (see Part 1); •, nonlinear numerical model with second-order closure (Newley 1986); ○, nonlinear numerical model with mixing length closure (Newley 1986); △, numerical model (Townsend 1972) ; ▼ numerical model (Townsend 1980).

become dynamically important in the lower part of the inner region and increase the total stress, hence, according to the physical picture developed in figure 5 of Part 1, the non-separated sheltering that induces the form drag is increased. The damped numerical model ($\alpha_d = 2$) gives a drag coefficient of 64.8 when $R = 3142$, which is amazingly close to the 62.8 measured by Zilker & Hanratty (1979) for $R = 2960$. In contrast, the undamped numerical model yields 84.7, almost 50% too large. The excellent agreement between the damped model and the experimental datum occurs because the numerical model includes the dynamical effect of viscous stresses in the inner region. This plot provides compelling evidence that the drag (and hence also the wave growth) is dependent on Reynolds number (in addition to the roughness and dimensionless wave speed). Notice that the range of R where the drag shows strong variation is within the range of R inferred from the Snyder *et al.* (1981) experiments, and so we expect that the growth rate of ocean waves will also depend on R.

4.1.3. *Comparisons with the coupled theory of Part 1*

In this section the predictions of the unconfined coupled numerical model are compared with the results of the coupled theory presented in Part 1. The first comparisons are given for the case $C_0 = 5$ and $kz_0 = 10^{-5}$, which is a 'slow wave' (as defined in Part 1) with $kl_a/(2\kappa^2) = 0.154$. The parameters of the numerical model were chosen to be $R = 3.02 \times 10^6$ and $Re_r = 2.4$, giving $kz_0 = \mathcal{K} Re_r/R = 10^{-5}$. Thus the base flow profile is fully rough and $Z_a^+ = 11\,800$ ($\gg 20$), as required. For this case the theory gives $kh_a = 0.344$ and a velocity scale $U_{0_a}/u_{*_a} = 22.0$ (see §5.3.1 in Part 1). The coupled base flow profile computed by the unconfined coupled model yields a velocity scale of $U_{0_a}/u_{*_a} = 19.0$; the difference reflects the difference between the
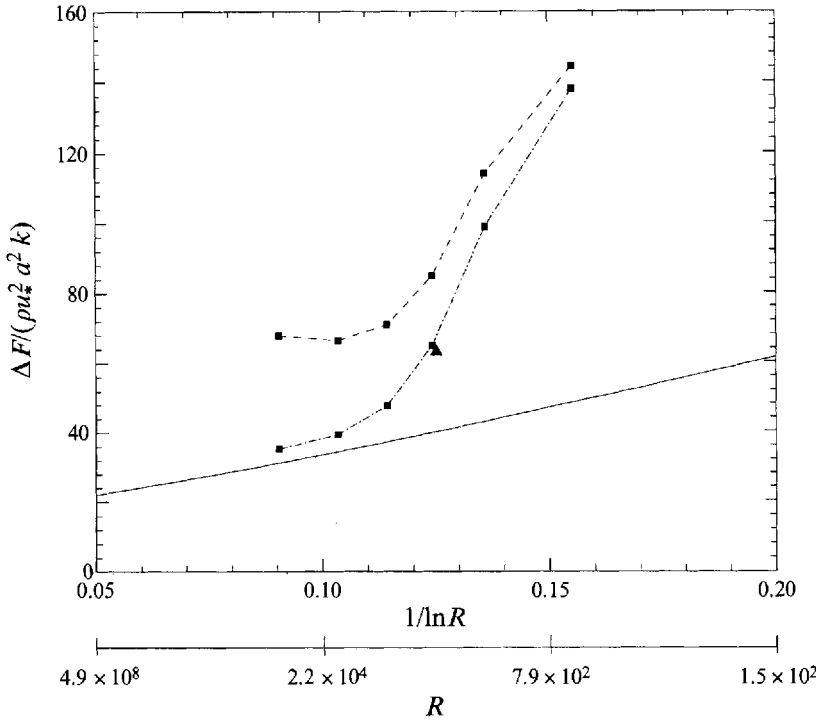
FIGURE 5. Effect of Reynolds number on the drag coefficient on a smooth sinusoidal hill: – ■ –, undamped model; —■—, damped model, $\alpha_d = 2$; ——, theory with truncated mixing length (modified theory of Belcher *et al.* 1993); ▲, experimental data of Zilker & Hanratty (1979).

R	Re_r	kz_0	$\Delta F/(\rho_a u_{*_a}^2 a^2 k)$			
			undamped	$\alpha_d = 2.0$	$\alpha_d = 1.0$	$\alpha_d = 0.5$
1.38×10^6	10	4.54×10^{-5}	80.47	38.67	34.69	33.71
4.55×10^5	10	1.38×10^{-4}	75.45	40.70	36.46	35.66
1.88×10^5	10	3.35×10^{-4}	71.28	42.11	37.65	37.05
9.05×10^4	10	6.94×10^{-4}	67.49	42.92	38.22	37.78
4.95×10^4	10	1.27×10^{-3}	63.94	43.03	38.24	38.00
2.95×10^4	10	2.13×10^{-3}	60.48	42.60	37.76	37.65
1.90×10^4	10	3.30×10^{-3}	57.18	41.78	36.95	36.97
1.30×10^4	10	4.83×10^{-3}	54.05	40.67	35.90	35.93
9.33×10^3	10	6.74×10^{-3}	51.11	39.44	34.71	34.71

TABLE 2. Computations of the form drag on a sinusoidal hill.

logarithmic base flow profile used in the theory and that computed by the present model. For the purposes of comparison the velocities and stresses were normalized using U_{0_a} rather than u_{*_a}, since this approach helps to remove the effect of slightly different base flow profiles.

Figures 6(*a*) and 6(*b*) show profiles of the horizontal velocity perturbation in the air above the interface. The velocity profiles at the wave crest (figure 6*a*) predicted by the numerical model and the theory are in good agreement except very near the interface. At the surface, the theory yields $\text{Re}(U_1) = 16.99$ at $kz = 10^{-5}$, whereas the numerical model predicts $\text{Re}(U_1) = 6.11$ at $kz = 0$, which is very close to the surface velocity

expected for an irrotational water wave ($\mathrm{Re}(U_1) \approx C + U_s = 6.1$). Such differences between the theory and the numerics in the near surface region could be due to their different treatment of the interface. The numerical model computes right down to the interface, whereas the theory stops at the roughness height, kz_0. Since the velocity profile is so steep directly above the interface, this small difference in height makes a relatively large difference in the predicted surface velocity.

The velocity profiles at the upwind wave slope (figure 6b) exhibit some differences. The numerical model predicts a peak in $\mathrm{Im}(U_1)/[U_{0_a}/u_{*_a}]$ of 0.623 at $kz = 7.3 \times 10^{-3}$, and then a sharp drop across the viscosity-affected region near the surface to match the near irrotational velocity (i.e. $\mathrm{Im}(U_1) \approx 0$) of the water wave. The theory predicts a peak value in $\mathrm{Im}(U_1)/[U_{0_a}/u_{*_a}]$ of 0.558 at $kz = 10^{-5}$ (in reasonable agreement with the magnitude of the peak predicted by the numerics) but no drop back to zero at the interface.

Figure 7 shows profiles of the perturbation shear stress computed by the numerical model (both damped and undamped) compared to the coupled theory of Part 1, in the near interface region on either side of the interface between $-0.4 \leqslant kz \leqslant 0.4$; the computational domain is $-2\pi \leqslant kz \leqslant 2\pi$. The height of the inner regions in the air and the water are $kz_a = 0.0492$ and $kz_w = 0.0050$, respectively, and the theoretical shear stress profiles are truncated at these points (for reasons explained in Belcher *et al.* 1993). The shear stress profiles at the wave crest (figure 7a) computed using the undamped model show extremely large values in the outer regions, most notably in the water where the stress reaches a peak of 0.125 at $kz = -1.00$! However, the damped model shows a shear stress that decays to zero, as it should in the outer region. The magnitudes of the peaks in the real part of the shear stress on either side of the interface from all models are in good agreement. Figure 7(b) shows that damping also has a lesser effect on the stress profile over the upwind slope, with similar trends as found for the hill flow in §4.1.1.

Although the profiles of the shear stress at the crest predicted by the theory and numerics demonstrate good agreement in both figure 3(a) and 7(a), the values of the shear stress at the *surface* show considerable differences, as evidenced in figure 8. This figure shows a plot of the surface shear stress at the wave crest predicted by the damped model compared with the coupled theory as a function of dimensionless wave speed, c_0/u_{*_a}, for various values of the roughness length, kz_0. For these computations the parameters of the numerical model were selected to be $Re_r = 2.4$ and $R = 3.02 \times 10^5$, 3.02×10^6 and 3.02×10^7, giving $kz_0 = 10^{-4}$, 10^{-5} and 10^{-6}, respectively. The numerical model consistently predicts lower values of surface shear stress than the coupled theory. Additionally, the theory predicts the surface shear stress to *decrease* with decreasing kz_0, whereas the numerics predict an *increase* with decreasing kz_0. However, both the theory and the numerics show that the surface shear stress decreases as a function of increasing wave speed. The apparent upturn in the surface shear stress predicted by the theory for large wave speeds should be viewed with caution: it is associated with the assumptions of the theory breaking down (e.g. at $kz_0 = 10^{-4}$ and $c_0/u_{*_a} = 10$ the value of $kl_a/(2\kappa^2)$ is 0.336, which is quite large). These differences may be due to the different treatments of the interface region. It is suprising that the differences are so large.

4.2. Confined flow

4.2.1. Comparisons with experimental wind-wave data

The coupled confined version of the numerical model is now applied to simulate the flow above and beneath mechanically generated water waves of frequency 1 Hz. Such
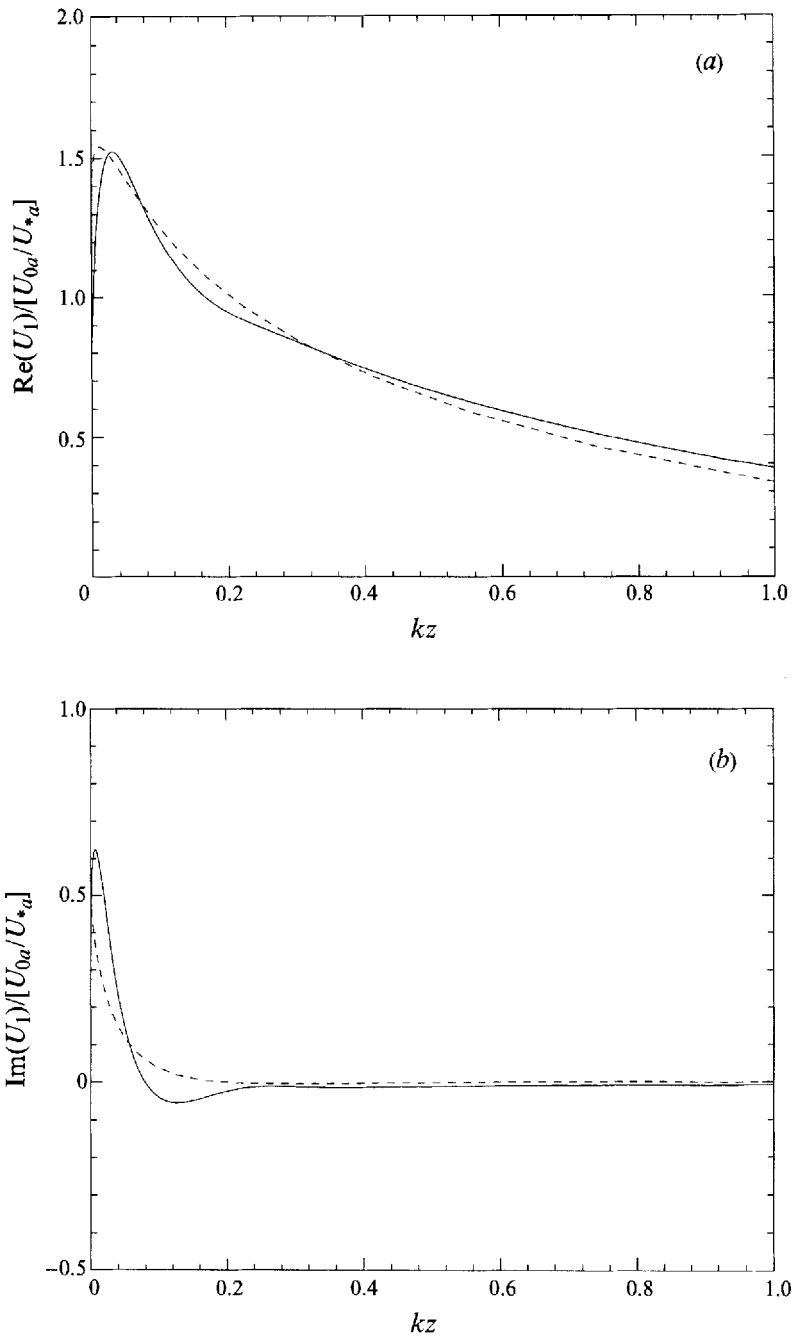
FIGURE 6. Profile of horizontal velocity perturbation above a water wave with $R = 10^5$, $Re_r = 10$ (so that $kz_0 = 10^{-5}$) and $C = 5$: (a) at the wave crest; (b) at the upwind slope. ——, Damped numerical model, $\alpha_d = 2$; - - -, theory with truncated mixing length (Part 1).
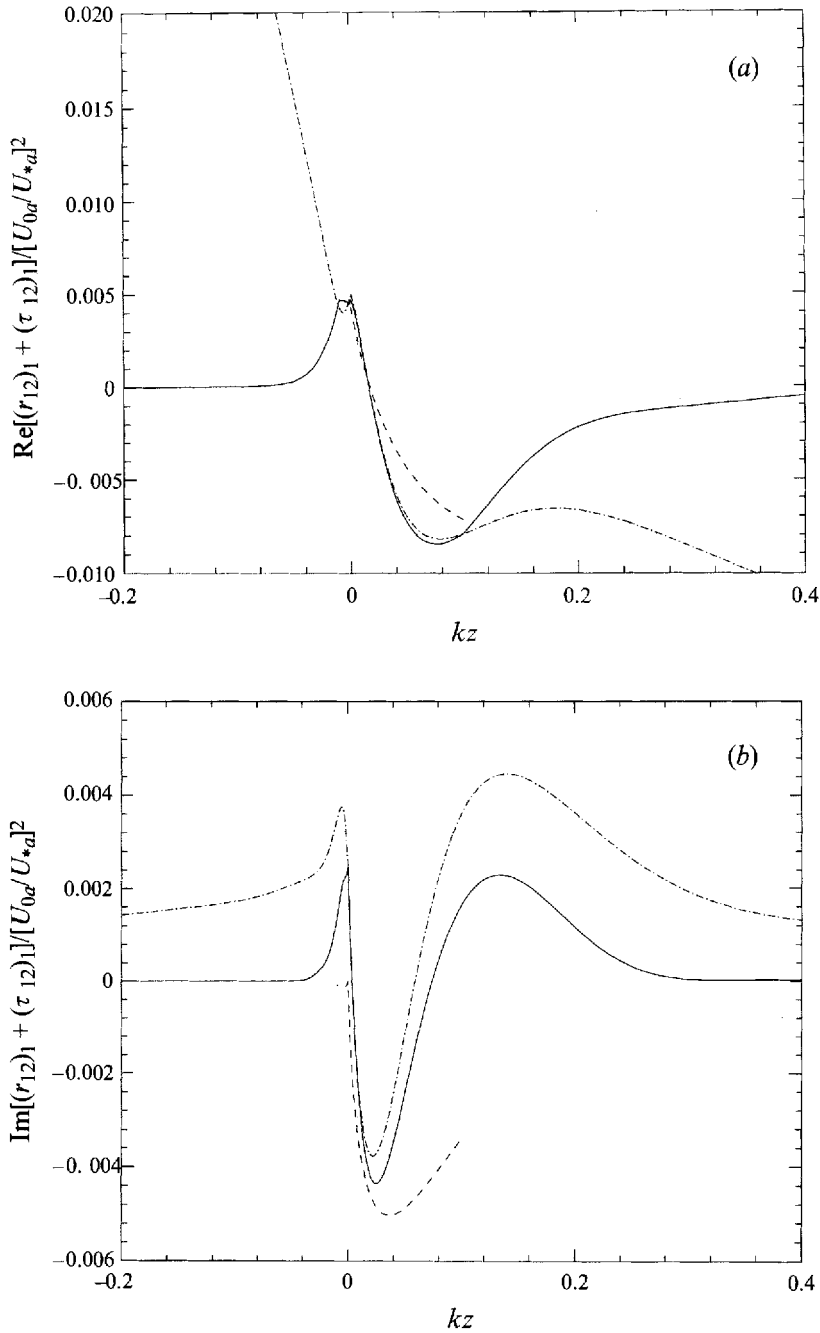
FIGURE 7. Profile of perturbation shear stress above and below a water wave with $R = 10^5$, $Re_r = 10$ (so that $kz_0 = 10^{-5}$) and $C = 5$: (a) at the wave crest; (b) at the upwind slope. ——, Damped numerical model, $\alpha_d = 2$; —·—, undamped numerical model; - - -, theory with truncated mixing length (Part 1).
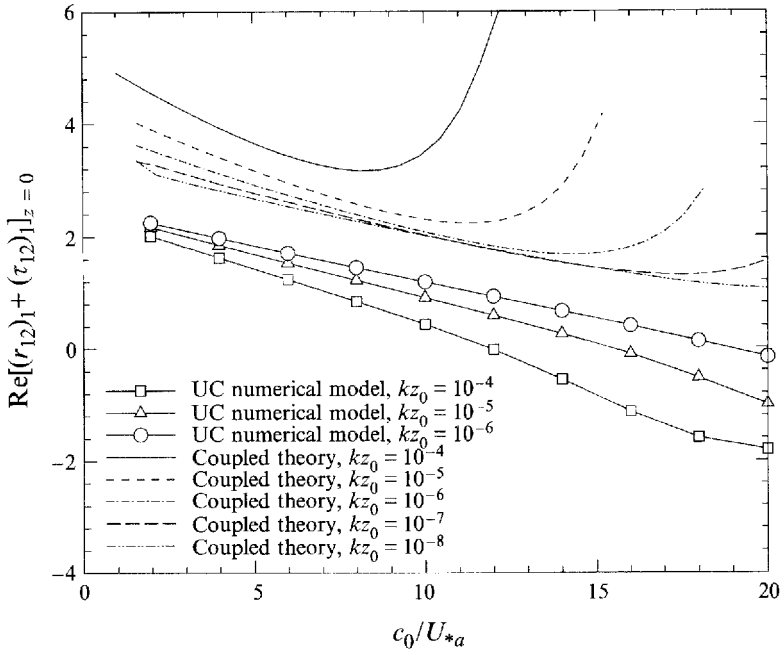
FIGURE 8. Surface shear stress perturbation at the wave crest as a function of dimensionless wave speed, c/u_{*_a}, and roughness length, kz_0.

Run	U_∞ (m s^{-1})	u_{*_a} (m s^{-1})	c/U_∞	ak	$R = 2Hu_{*_a}/\nu$	$\alpha_+ = \mathcal{K}/R$
1	1.37	0.043	1.14	0.106	5560	1.40 x 10^{-3}
2	1.72	0.056	0.91	0.107	7240	1.08 x 10^{-3}
3	2.12	0.073	0.74	0.105	9440	8.26 x 10^{-4}
I	2.40	0.085	0.65	0.107	11020	7.08 x 10^{-4}
4	2.92	0.110	0.53	0.115	14220	5.49 x 10^{-4}

TABLE 3. Parameters of Hsu & Hsu (1983) experiments. The dimensionless wavelength based on $2H$ is $\mathcal{K} = 2kH = 7.80$ ($H = 1.97$ m).

waves were studied in the Stanford Wind Water-Wave Research Facility (SWWWRF) by Hsu & Hsu (1983), who measured profiles of velocity and shear stress in the air at free-stream wind speeds of $U_\infty = 1.37$, 1.72, 2.12 and 2.92 m s^{-1}.

Table 3 summarizes the parameters of the experiments performed by Hsu & Hsu (including the case of Hsu *et al.* 1981, denoted by Run I). The runs cover the ranges of dimensionless wave speeds and inverse Reynolds numbers ($\alpha_+ = k\nu_a/u_{*_a}$) that are particularly sensitive to the choice of Reynolds stress model (Harris & Street 1994). Thus they represent a challenging test of the present numerical model.

One difficultly in simulating these experiments is that Hsu & Hsu (1983) obtained values for the friction velocity from *time-averaged* velocity profiles. The 1 Hz mechanically generated wave causes these time-averaged profiles to be contaminated by second-order (in ak) perturbation components as noted in Part 1, §2. Evidence for this contamination may be seen in Hsu & Hsu figure 2 which shows that the time-averaged velocity profiles exhibit 'super smooth' behaviour when plotted in

Run	R	U_∞/u_{*_a}	U_s/u_{*_a}	U_s/U_∞	C	$(c/u_{*_a})_{expt}$
1	5560	24.72	0.7580	0.0307	28.2	36.3
2	7240	25.34	0.7794	0.0308	23.1	27.9
3	9440	25.95	0.8009	0.0309	19.5	21.4
I	11020	26.32	0.8122	0.0309	17.1	18.2
4	14220	26.92	0.8340	0.0310	14.3	14.2

TABLE 4. Computed parameters for Hsu & Hsu (1983) experimental runs

law-of-the-wall coordinates; this behaviour does not occur in the absence of the mechanically generated wave component. Thus, the friction velocities quoted by Hsu & Hsu are not consistent with the definition of the base flow in the present model. The most significant effect of this error is manifested in the values of c/u_{*_a} quoted by Hsu & Hsu. The following correction procedure is adopted: (i) calculate a Reynolds number, R, using the measured value of u_{*_a}; (ii) solve the numerical model for the base flow using the calculated value of R; (iii) obtain the value of U_∞/u_{*_a} (equal to the dimensionless free-stream velocity, U_0, at mid-channel height in the air) from the results of the computation; and (iv) calculate $C = c/u_{*_a} = (c/U_\infty)(U_\infty/u_{*_a})$, where c/U_∞, given in table 3, is measured experimentally and is assumed to be reliable. Of course, this procedure could be continued to produce corrections to the Reynolds number. However, this was not considered necessary since the results of the numerical model are insensitive to such small changes in the Reynolds number. Hsu & Hsu state that in all cases the flow is hydraulically smooth ($Re_r \leqslant 0.12$). This is not strictly true for the corrected u_{*_a} values, but the computations of Harris & Street (1991) show that, at the low wind speeds used by Hsu & Hsu (1983), the flow is hydraulically smooth except for Run 4 where it is transitional.

Table 4 summarizes the values of U_∞/u_{*_a} and other parameters computed for the Hsu & Hsu runs using the coupled confined base flow model. As can be seen, the values of $C = c/u_{*_a}$ obtained from the model using the above procedure differ from the experimental values quoted by Hsu & Hsu (1983), especially for the low wind speeds. Table 4 also shows the computed surface drift velocities, U_s/u_{*_a}, where U_s is the mean velocity at the air–water interface (i.e. $U_0(Z = 0)$). Converting these values to U_s/U_∞ using the computed values of U_∞/u_{*_a} reveals that the drift velocity is almost exactly 3% of the free-stream wind speed for all runs. This computed value is consistent with the experimentally observed values of about 3% of the free-stream wind speed reported by Shemdin (1976), which gives us further confidence in the numerical model of the base flow.

An example of the base flow velocity profiles computed by the confined coupled model for a free-stream wind speed of $U_\infty = 2.92$ m s^{-1} (Hsu & Hsu run 4) is shown in figure 9. The profiles in the air and the water are shown in separate plots since the velocities in the water are considerably smaller than those in the air. The non-zero velocity at the interface (i.e. the drift velocity) may clearly be seen. As mentioned in Appendix A, there is no net flow in the water since the water channel in the SWWWRF is finite in length and, consequently, the drift current beneath the interface induces a return flow along the channel bottom. The base flow profiles for the other wind speeds are qualitatively similar.

The next step in the simulations of the Hsu & Hsu experiments involved running the confined coupled version of the perturbation model using the tabulated Reynolds
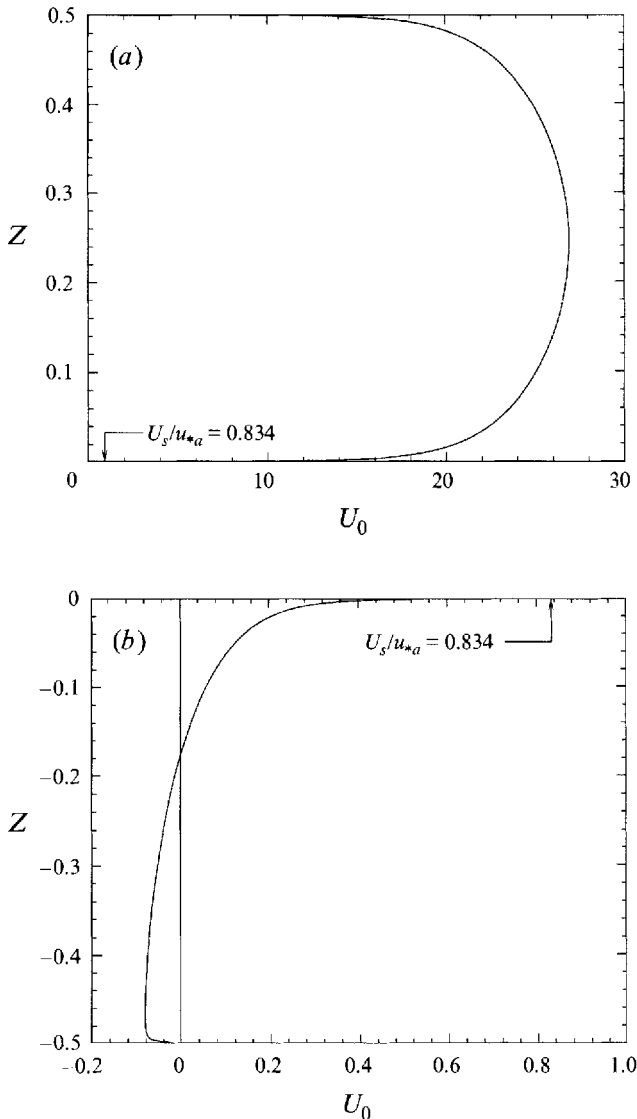
FIGURE 9. Computed profile of confined coupled base flow in the SWWWRF for $U_\infty = 2.92$ m s^{-1} (Hsu & Hsu run 4): (a) in the air; (b) in the water.

numbers and dimensionless wave speeds as parameters (along with $Re_r = 0.11$, $\mathcal{K} = 7.80$ and $\alpha_d = 2.0$). The initial guess for $\mathrm{Re}(C)$ was chosen so that the final converged value of $\mathrm{Re}(C)$ was equal to the required value, shown in table 4, to within less than 1%.

Figures 10 and 11 show profiles of horizontal and vertical velocity perturbations in the vicinity of the air–water interface over a range of wind speeds compared to the experimental values measured by Hsu & Hsu (1983). The experimental data were obtained from figures 3 and 4 in Hsu & Hsu (1983), converted to real and imaginary components and converted to the present notation using the experimental values of ak and the computed values of U_∞/u_{*_a} given in table 4.

Figure 10 shows reasonable agreement between the modelled and measured horizontal velocity perturbations at both the crest (a) and the upwind slope (b). There
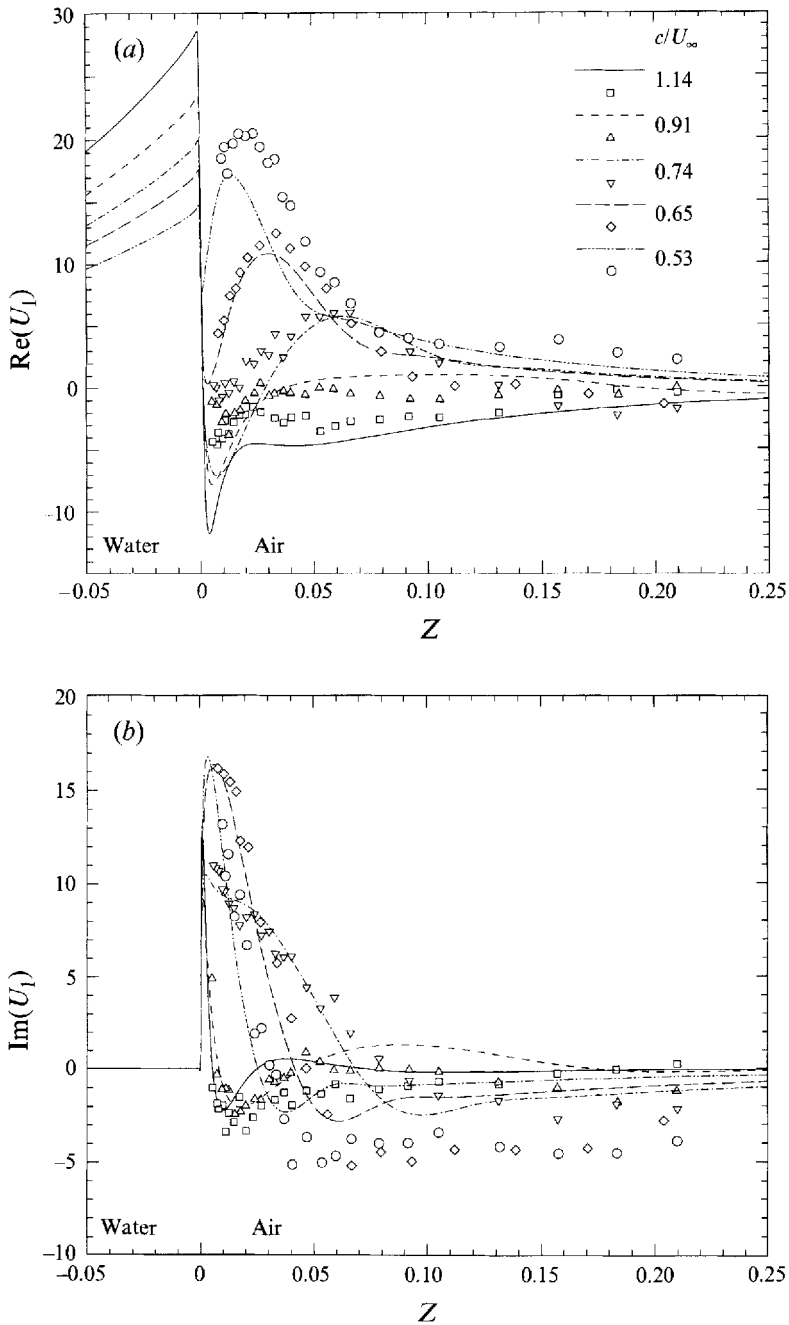
FIGURE 10. Profiles of the horizontal velocity perturbation in the vicinity of the air water interface computed with the damped numerical model(curves) and comparisons with the experimental data of Hsu & Hsu (1983)(symbols): (*a*) at the wave crest; (*b*) at the upwind wave slope.
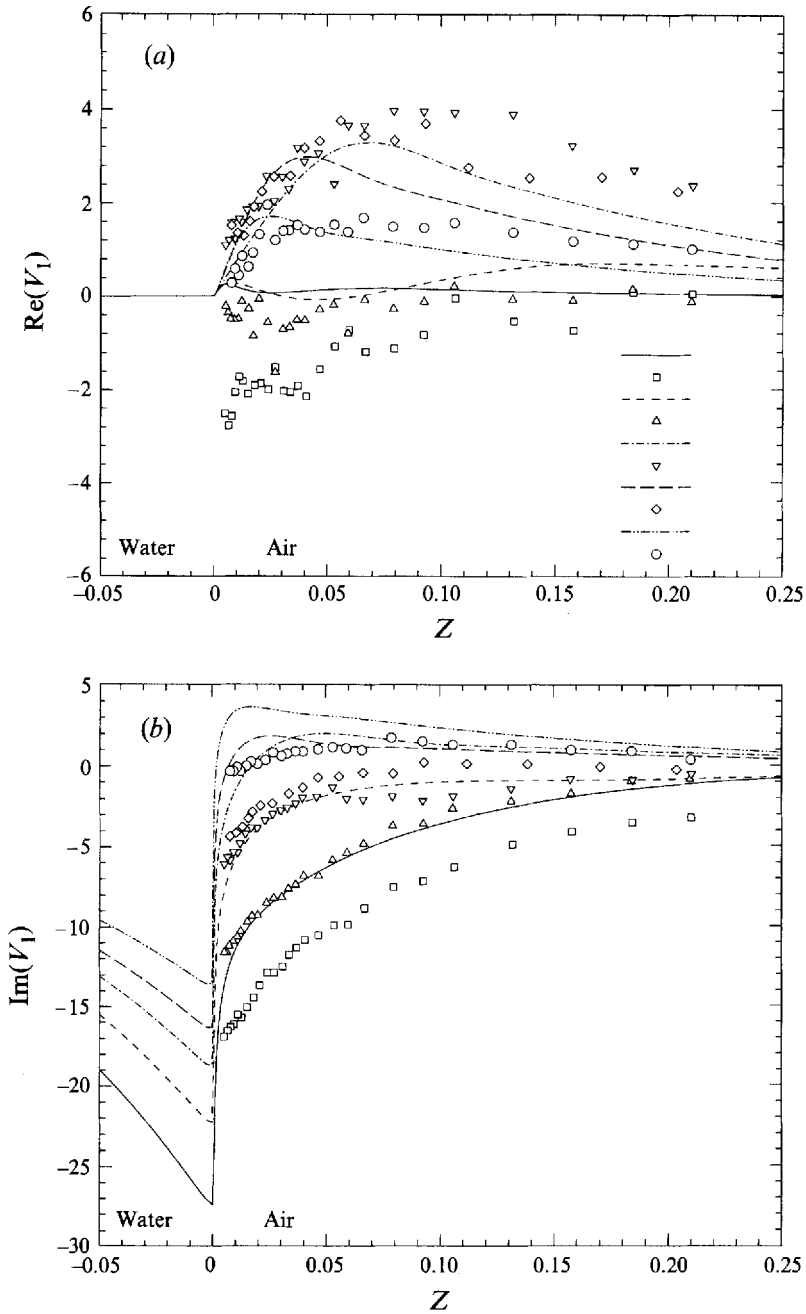
FIGURE 11. Profiles of the vertical velocity perturbation in the vicinity of the air–water interface computed with the damped numerical model(curves) and comparisons with the experimental data of Hsu & Hsu (1983)(symbols): (a) at the wave crest; (b) at the upwind wave slope.

are significant changes in the shape of the horizontal velocity perturbation as c/U_∞ (and, to a lesser extent, R) varies, which are well-captured by the model. For the three slower-moving waves ($c/U_\infty = 0.53$, 0.65 and 0.74) and close to the interface ($Z \lesssim 0.5$), the model agrees with the data to within about 25%. For the faster-moving waves ($c/U_\infty = 0.91$ and 1.14), the qualitative agreement is good, but the quantitative agreement deteriorates. In all cases the agreement between the experimental data and the model is better near the surface than in the outer part of the flow. The measurements were made at a relatively short fetch of 13 m, so that the base flow boundary layer might be expected to be well developed up to a height of about $h \sim 13/50 \approx 0.25$ m, which implies that $kh \sim 1$. Hence the outer part of the flow may not be well developed.

As mentioned by Hsu & Hsu, the experimental data do not seem to approach the values at the surface that would be given by an irrotational water wave (i.e. $\mathrm{Re}(U_1) \approx C$ and $\mathrm{Im}(U_1) \approx 0$ at $Z = 0$). However, the data are consistent with the model, and the model shows that the water motions are close to irrotational (except very near the interface), and that the velocity profiles in the air have a huge shear in the immediate vicinity of the water surface. For example, when $c/U_\infty = 1.14$, $\mathrm{Re}(U_1) \approx -12$ just above the interface but $\mathrm{Re}(U_1) \approx 29$ just below the interface.

It is unlikely that these rapid velocity variations are associated with a critical layer, where $U_0(Z) = C$, because the present calculations show that they persist even for $c/U_\infty > 1$, when there is no critical level. In fact, much of the shear seems to lie in a zone that scales with the molecular viscosity: in all runs the shear is located below $Z \lesssim 0.005$, which corresponds to $z^+ \lesssim 50$ (using a representative value of $R = 10\,000$). Another viscous length scale is the thickness of the Stokes layer, $l_v = (\omega/2\nu_a)^{-1/2}$ (where ω is the wave radian frequency), which gives $z^+ \approx 11$ in the Hsu & Hsu experiments. To test this idea, figure 12 shows the effect of Reynolds number on model profiles of the horizontal velocity pertubation for $c/U_\infty = 0.91$. The Reynolds numbers are chosen to be $R = 7240$ (the actual case) and $R = 50\,000$ and the depths of the inner region, Z_a, critical layer, Z_c and viscous sublayer, Z_v, are all marked. Changing R changes the base flow so the velocity is scaled by u_{*_a}/U_∞, which has the values 25.34 and 29.88 for $R = 7240$ and $50\,000$ respectively. The height of the Stokes layer is constant and lies at $Z = 1.1 \times 10^{-3}$. The large change in Reynolds number does not greatly influence the magnitude of the velocity perturbations. But most of the shear in $\mathrm{Re}(U_1)$ does occur within the viscous sublayer and moves considerably closer to the interface at the higher Reynolds number. In contrast, the shear in $\mathrm{Im}(U_1)$ seems to remain at the Stokes layer height for both Reynolds numbers. From this plot it is also apparent that the critical layer does not play a role in causing the rapid variation in velocity near the interface, at least for this run. This plot suggests that molecular viscosity is important in coupling the air and water motions.

Figure 11(a) shows the measured and predicted profiles of the real part of the vertical velocity perturbation. The trends in the comparison are similar to those found for the horizontal velocity, with good quantitative agreement near the interface ($Z \lesssim 0.05$) and for the three slower-moving waves. The numerical model does not give the observed negative values of $\mathrm{Re}(V_1)$ for $c/U_\infty = 1.14$, possibly because the corrected value of c/u_{*_a} is so different to the measured value in this case (i.e. the true value of C may lie somewhere in between the corrected and uncorrected values). Figure 11(a) shows that the coupled numerical model is in close agreement with irrotational water wave theory, which gives $\mathrm{Re}(V_1) = 0$ at the interface.

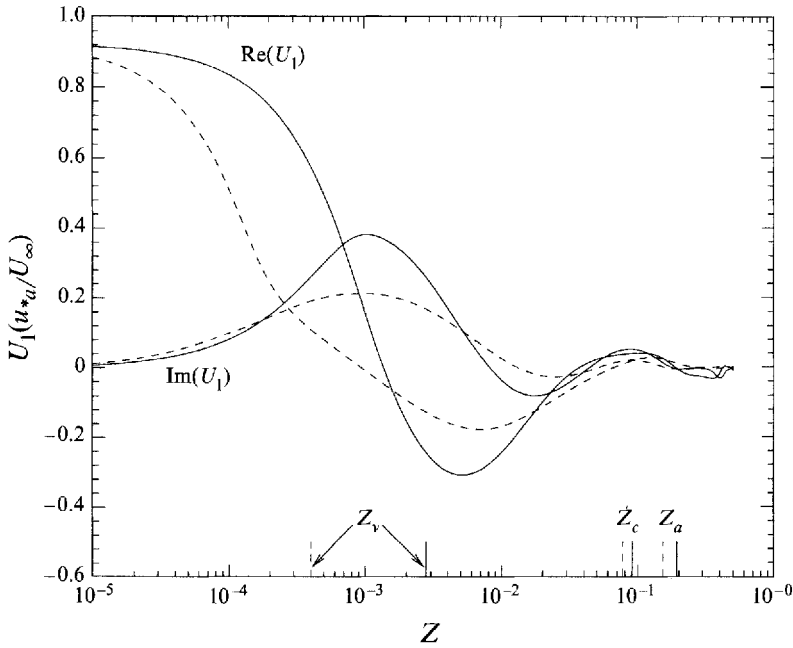Figure 11(b) shows a comparison of calculated and measured profiles of the imag-

FIGURE 12. Effect of Reynolds number on profiles of the horizontal air flow perturbation above a water wave ($c/U_\infty = 0.91$) computed with the damped model: ——, $R = 7240$ (Hsu & Hsu run 2); - - -, $R = 50000$. The labels Z_a, Z_c and Z_v mark the depths of the inner region, critical layer and viscous sublayer, respectively.

inary part of the vertical velocity perturbation. There is good qualitative agreement, but the numerical values are systematically larger than the measured values, despite the small scatter in the data. The reason for these systematic differences is not clear: it could be due to uncertainty in the value of u_{*_a}, which influences the value of C as well as the scaling of the profiles. The numerical model predicts $\mathrm{Im}(V_1) \approx -C$ at the interface (in agreement with irrotational water wave theory).

The performance of the numerical model in predicting the measured perturbation velocity profiles for this challenging problem is encouraging. However, model valida-tion using only perturbation velocity profiles for comparison is not really sufficient for a wave growth model since, away from the interface, the velocity profiles are determined largely by inviscid dynamics and are not particularly sensitive to the perturbation Reynolds stress model (Belcher & Hunt 1993).

So figure 13 shows a comparison of the predicted and measured perturbation shear stress profiles for the cases studied by Hsu & Hsu (1983) and Hsu et al. (1981). The experimental data were obtained from figure 7 in Hsu & Hsu (1983), converted to real and imaginary components and scaled by $ak(U_\infty/u_{*_a})^2$ to convert to the present notation. Figure 13(a) shows that for the two slower-moving waves the coupled numerical model agrees with the measured $\mathrm{Re}[(r_{12})_1]$ profiles to within about 10% throughout the inner regions, i.e. $Z \lesssim 0.07$. In the outer regions we do not expect good agreement because the turbulence is changed by rapid distortion, which is not modelled in detail in the damped eddy viscosity model. For the faster-moving waves, the agreement deteriorates. This is suprising because as c/U_∞ increases so the inner-region depth increases and we might expect good agreement over the whole depth of the air. Instead when $c/U_\infty = 1.14$ the model shows a large negative

stress perturbation, whereas the data show a near zero perturbation. This trend is observed in the comparisons of the velocity profiles and suggests that the model may not adequately model waves moving faster than the wind. Figure 13(b) shows the computed profiles of $Im[(r_{12})_1]$, which do not agree as well with the experimental data. The numerical model tends to underpredict the peak in the measured $Im[(r_{12})_1]$ component near the interface over the whole range of c/U_∞. For the two highest values of c/U_∞ the numerical model also predicts negative values of $Im[(r_{12})_1]$ which are not observed experimentally. It is likely that this discrepancy in the predicted and measured profiles of $Im[(r_{12})_1]$ is due to the limitations of the isotropic eddy viscosity model for the perturbation shear stresses in the parameter range around $\alpha_+ \approx 10^{-3}$ as well as for the other reasons outlined above.

For a hydraulically smooth interface the surface value of $(r_{12})_1$ must be zero and the model profiles show this behaviour. However, in most cases the measured profiles show a consistent increase near the interface which appears to contradict this result. The measured data are not generally close enough to the interface to capture this behaviour in the inner region except in the case $c/U_\infty = 0.65$ where a decrease in the measured value of $Im[(r_{12})_1]$ near the interface is apparent.

5. Summary and conclusions

We have developed a numerical model of the fully developed turbulent air flow above and water flow below a travelling surface wave. First the model computes the base flow (i.e. the flow over and under a flat interface), and secondly the model computes linear perturbations to the base flow caused by a wave of low slope, i.e. $ak \lesssim 0.1$. The model accounts for the fully turbulent drift current in the water, and there is full dynamical coupling to the air flow above. The model uses a new *damped eddy viscosity* turbulence parameterization for the wave-induced stresses, which accounts for the regions of rapid distortion of the turbulence. In addition the model accounts for effects of low turbulence Reynolds number, which has allowed us to assess the role in wind–wave interactions of the viscous sublayer around the interface.

An advantage of decomposing into base and perturbation flows is that we were able to incorporate into a new damped eddy viscosity model the results of scaling arguments developed by Townsend (1980), Belcher *et al.* (1993), Belcher & Hunt (1993) and in Part 1. Thus the wave-induced Reynolds stress was modelled using an eddy viscosity that was multiplied by a damping function, f_d. The scaling arguments indicate that f_d is a function of Z/l, where l is the inner-region length scale (defined in §§4.3 and 4.5 of Part 1), and that in both the air and water $f_d \to 0$ as $|Z/l| \to \infty$ and $f_d \to 1$ as $Z/l \to 0$. Thus the model makes explicit use of results from linear analysis. Here f_d was taken to be an exponential decay, with a damping coefficient α_d (see equation (2.20)). We then reasoned that, according to the linear analysis developed in Belcher & Hunt (1993) and Part 1, if the stress perturbation profile at the wave crest is modelled accurately, then the form drag and wave growth should also be accurate. Hence α_d was calibrated by comparing computed profiles of the stress perturbation with profiles computed by Newley (1986) using a second-order closure. It is gratifying that the values of the form drag on a rigid stationary sinusoidal wave computed with the new model then agree well with the results computed with the second-order closure, particularly when the form drag is so sensitive to closure (Belcher *et al.* 1993; Xu & Taylor 1995). Some aspects of the flow are clearly sensitive to the choice of f_d and α_d, and further work needs to be done to improve the modelled values of
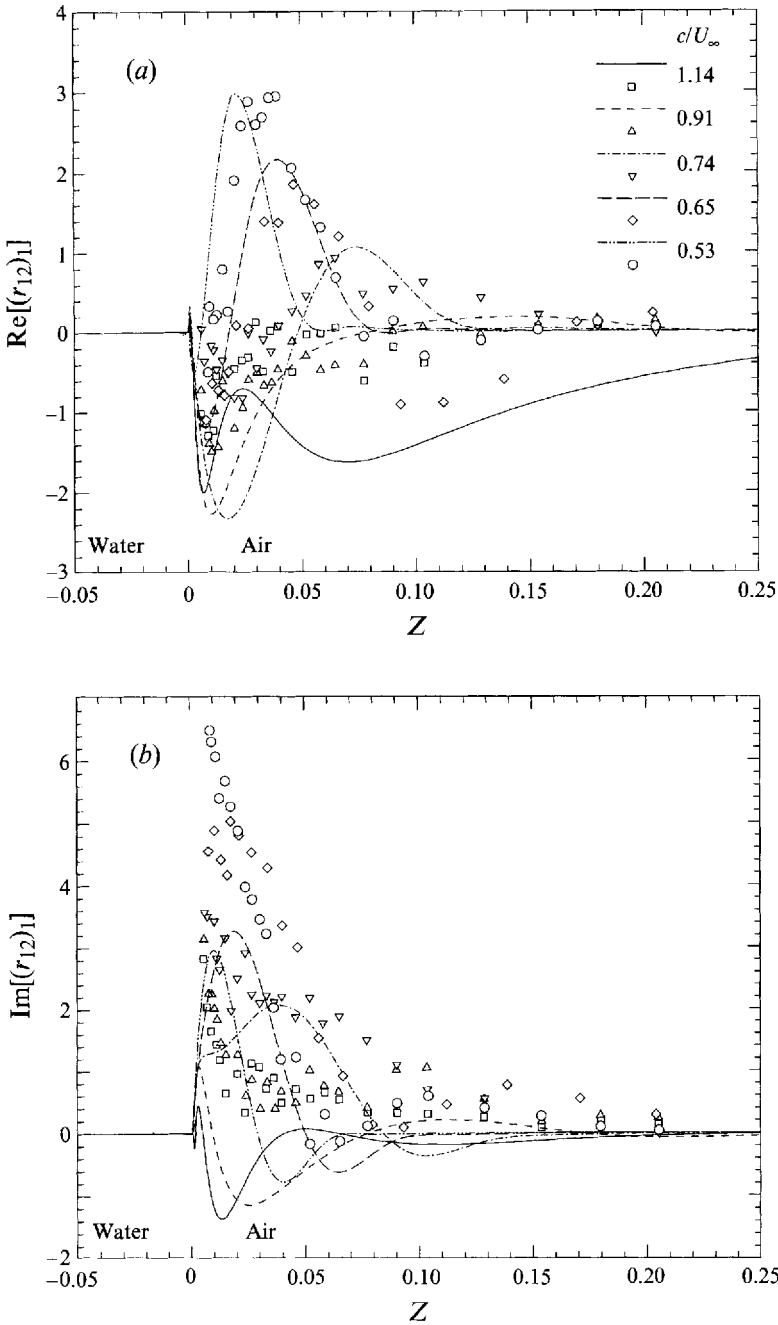
FIGURE 13. Profiles of the shear stress perturbation in the vicinity of the air–water interface computed with the damped numerical model(curves) and comparisons with the experimental data of Hsu & Hsu (1983)(symbols): (*a*) at the wave crest; (*b*) at the upwind wave slope.

the imaginary part of the shear stress, but the form drag, and hence wave growth rate, is rather insensitive to the value of α_d provided it is small enough to damp effectively outside the inner regions. Further work also needs to be done to formulate a nonlinear version of the model.

We have shown that in the air flow when $R \lesssim 2 \times 10^4$ the depth of the viscous sublayer is comparable with the depth of the inner region, which is where turbulent stresses are dynamically important. It is clear that in such conditions viscous stresses may be dynamically important. In the water flow, the depth of the inner region is comparable to, or even less than, the depth of the viscous sublayer for most of the values of R observed. Hence, viscous stresses may even dominate over the turbulent stresses in the wave-induced water flow, at least when the turbulence is shear driven (rather than from wave breaking). The effect of viscous sublayers is manifested in the variation of the form drag with R. When $R \gtrsim 2 \times 10^4$ the form drag agrees well with the analytical model of Belcher *et al.* (1993), which assumes that viscous stresses play no dynamical role in the inner region. But when $R \lesssim 2 \times 10^4$, which is within the range observed in the wind waves observed in the field by Snyder *et al.* (1981), the form drag increases rapidly with decreasing R (by a factor of about two as R drops by a factor of ten). With the new model the calculated value of the form drag agrees with the value measured by Zilker & Hanratty (1979) to within 5%, but this is almost 50% larger than the value computed without accounting for the dynamical effects of viscosity. It would be extremely interesting to have more data to compare with this aspect of the model.

The numerical model was compared in detail with the measurements of Hsu & Hsu (1983), which were made over waves that spanned the intermediate and fast-moving regimes and a case where the wave travelled faster than the wind. We showed that the values of u_{*a} reported by Hsu & Hsu (1983) were not the same as the base flow values that are needed as input to the model and so we described a correction procedure. It seems likely that other comparisons between models and data need to adopt a similar procedure. For the intermediate cases, $c/U_\infty = 0.53$, 0.65 and 0.74, the profiles of $\mathrm{Re}\{U_1\}$ and $\mathrm{Re}\{\tau_1\}$ computed with the model agreed well with the data, particularly in the near-wall region, $Z \lesssim 0.05$ m. A possible explanation for the poorer agreement above this height is that the measurements were made at a relatively short fetch of 13 m, so that the outer part of the flow may not have been be well developed. Another possibility, in the stress comparisons, is that in the outer region of the wave-induced flow the turbulence is subjected to rapid distortion, which we have modelled as being zero in the damped eddy viscosity model. Hence the wave-induced stress profiles have small changes that are not accounted for explicitly in the present turbulence model. For the waves travelling faster than the wind, the model does not agree so well with the measured profiles. The agreement deteriorates as c/U_∞ increases, so it may be that the present model is lacking some physical process that is important for these very fast-moving waves.

The present approach to modelling wind waves has forced us to focus on the near-interface region. The scaling arguments put forward by Belcher *et al.* (1993) show that effects of turbulent stresses on the wave-induced flow are confined to inner regions. And in the present paper we have shown that a role can be played by molecular viscosity, which is dynamically important in even thinner viscous sublayers either side of the interface. Evidence of the importance of these viscous layers is in the profiles of wave-induced streamwise velocity, which have a large shear confined within the viscous sublayers. These findings are of significance to high-resolution numerical

simulations, such as direct numerical simulation or large-eddy simulation, which would have to account for these extremely small-scale processes. The comparisons with the Hsu & Hsu data show that these considerations are relevant to wind-ruffled mechanically generated waves. But what can these results tell us about pure wind-generated waves? In such flows the interface is highly contorted so that it is not clear how to define the interface down to scales of millimetres. It is certainly extremely difficult (impossible?) to make measurements within the viscous sublayers in the real flow. Perhaps the main value of this work is the most general conclusion, namely that the details of smallest scales of the air and water flows in the close vicinity of the interface can have an order-one effect on the dynamics of the dominant wave (perhaps by doubling its growth rate). We shall quantify some of these effects in more detail and make further comparisons with the theory of Part 1 in Part 3 of our study (Belcher, Harris & Street 1996).

Appendix A. Boundary conditions

The boundary conditions for the base flow equations are summarized in table 5. Note that the definition of Z is different in each case (refer to table 1). For confined flow the confining surfaces are considered to be smooth and no-slip boundary conditions are used: $U_B = K_B = \tilde{E}_B = 0$. For unconfined flow the far-field boundary conditions are assumed to be given by the logarithmic law so that the turbulent kinetic energy and dissipation rate are given by the wall functions used in standard $k - \varepsilon$ models, which may be expressed as (ASCE Task Committee on Turbulence Models in Hydraulic Computations 1988)

$$K_B = 1/(\mathscr{P}c_\mu^{1/2}), \quad \tilde{E}_B = 1/(\kappa\mathscr{P}^{3/2}|Z|) \quad \text{at the domain limits.} \tag{A 1}$$

Uncoupled flows also require boundary conditions at the air–water interface, where the base flow velocity is assumed to be the surface drift velocity, U_s, which is taken to be 3% of the free-stream wind speed as measured by Shemdin (1976). The interfacial roughness is characterized by a roughness length, z_0, which, for simplicity, is taken to be the same in the air and the water (Kondo 1976). Harris & Street (1991) and Harris (1992) show that the interfacial values of K_B and $\tilde{E}_B$ (denoted by K_s and $\tilde{E}_s$) in the air and water may be computed by

$$K_s(R, Z_0) = \frac{1}{4\kappa^2 Z_0^2 c_\mu^{1/2}} \left(-\mathscr{V}/R + [(\mathscr{V}/R)^2 + 4\kappa^2 Z_0^2/\mathscr{P}]^{1/2}\right)^2, \tag{A 2}$$

$$\tilde{E}_s(R, Z_0) = c_\mu^{3/4} K_s^{3/2} f_\mu(K_s, \tilde{E}_s)/\kappa Z_0, \tag{A 3}$$

Case	Domain	Lower b.c.	Upper b.c.	Auxiliary condition
CU	$0 \leqslant Z \leqslant 1$	$U_B = U_s$ $K_B = K_s(R, Z_0)$ $\tilde{E}_B = \tilde{E}_s(R, Z_0)$	$K_B = 0$ $\tilde{E}_B = 0$	Choose $\partial P_B/\partial X$ s.t. $U_B(1) = 0$
CC	$-\frac{1}{2} \leqslant Z \leqslant \frac{1}{2}$	$U_B = 0$ $K_B = 0$ $\tilde{E}_B = 0$	$K_B = 0$ $\tilde{E}_B = 0$	Choose $\partial P_B/\partial X_a$ and $\partial P_B/\partial X_w$ s.t. $U_B(\frac{1}{2}) = 0$ and $\int_{-1/2}^{0} U_B(Z)\,dZ = 0$
UU	$0 \leqslant Z \leqslant 1$	$U_B = U_s$ $K_B = K_s(R, Z_0)$ $\tilde{E}_B = \tilde{E}_s(R, Z_0)$	$K_B = 1/c_\mu^{1/2}$ $\tilde{E}_B = 1/\kappa|Z|$	$\partial P_B/\partial X = 0$
UC	$-\frac{1}{2} \leqslant Z \leqslant \frac{1}{2}$	$U_B = 0$ $K_B = 1/\mathscr{P}c_\mu^{1/2}$ $\tilde{E}_B = 1/\kappa\mathscr{P}^{3/2}|Z|$	$K_B = 1/c_\mu^{1/2}$ $\tilde{E}_B = 1/\kappa|Z|$	$\partial P_B/\partial X_a = 0$ $\partial P_B/\partial X_w = 0$

TABLE 5. Summary of boundary conditions for the base flow solution.

where $Z_0 = z_0/\mathscr{L}$. Then K_s and $\tilde{E}_s$ are different on the air and water sides of the interface since the roughness Reynolds number in the air is about twice that in the water. In confined flow, auxiliary conditions are required to determine the pressure gradients. The pressure gradient in the air is determined by the auxiliary condition that the velocity at the upper boundary vanishes. For coupled flow the pressure gradient in the water is chosen to produce no net flow in the water, since the water channel is finite in length and the drift current must recirculate.

A summary of the perturbed flow boundary conditions is presented in table 6. For confined flow the perturbation quantities vanish at the confining walls according to the no-slip condition. For uncoupled flow the boundary conditions on the perturbation velocities at the interface are given by (Hsu *et al.* 1981)

$$U_1 = C + U_s, \quad V_1 = \mathrm{i}(U_s - C) \quad \text{at } Z = 0. \tag{A 4}$$

K_1 and $\tilde{E}_1$ were set to zero at the air–water interface, which corresponds to specifying a constant roughness along the wave. We use this condition because Gent & Taylor (1976) and Belcher & Hunt (1993) have shown that a varying z_0 along the wave has only a second-order effect on the flow. In unconfined flow, far from the interface the perturbed quantities are forced to decay exponentially. The solution technique outlined in §3 only uses the derivative of the continuity equation; thus, to ensure the continuity equation returns zero (and not some other constant) the continuity condition is imposed at the boundary.

Appendix B. Coupling conditions

The kinematical and dynamical coupling conditions are transformed and expanded, then terms of order zero and one in the wave slope are selected for the base and perturbed flow (Harris 1992).

The zeroth-order component of the kinematical and dynamical conditions for the

Case	Domain	Lower b.c.	Upper b.c.
CU	$0 \leqslant Z \leqslant 1$	$U_1 = C + Us$ $V_1 = i(U_s - C)$ $K_1 = 0$ $\tilde{E}_1 = 0$ $i\mathcal{K}U_1 - ifU'_B + V'_1 = 0$	$U_1 = 0$ $V_1 = 0$ $K_1 = 0$ $\tilde{E}_1 = 0$
CC	$-\frac{1}{2} \leqslant Z \leqslant \frac{1}{2}$	$U_1 = 0$ $V_1 = 0$ $K_1 = 0$ $\tilde{E}_1 = 0$ $i\mathcal{K}U_1 - ifU'_B + V'_1 = 0$	$U_1 = 0$ $V_1 = 0$ $K_1 = 0$ $\tilde{E}_1 = 0$
UU	$0 \leqslant Z \leqslant 1$	$U_1 = C + U_s$ $V_1 = i(U_s - C)$ $K_1 = 0$ $\tilde{E}_1 = 0$ $i\mathcal{K}U_1 - ifU'_B + V'_1 = 0$	$U'_1 = \mathcal{K}U_1$ $V'_1 = \mathcal{K}V_1$ $K'_1 = \mathcal{K}K_1$ $\tilde{E}'_1 = \mathcal{K}\tilde{E}_1$
UC	$-\frac{1}{2} \leqslant Z \leqslant \frac{1}{2}$	$U'_1 = -\mathcal{K}U_1$ $V'_1 = -\mathcal{K}V_1$ $K'_1 = -\mathcal{K}K_1$ $\tilde{E}'_1 = -\mathcal{K}\tilde{E}_1$ $i\mathcal{K}U_1 - ifU'_B + V'_1 = 0$	$U'_1 = \mathcal{K}U_1$ $V'_1 = \mathcal{K}V_1$ $K'_1 = \mathcal{K}K_1$ $\tilde{E}'_1 = \mathcal{K}\tilde{E}_1$

TABLE 6. Summary of boundary conditions for the perturbed flow solution.

base flow yield

$$[U_B] = 0, \quad \left[\mathcal{P} \left(\frac{\mathcal{V}}{\mathcal{R}} + \bar{v}_{t_B} \right) \frac{\partial U_B}{\partial Z} \right] = 0 \quad \text{at } Z = 0, \tag{B1}$$

where $[q]$ denotes the value of q on the air side of the interface minus the value of q on the water side of the interface. The second result can be written $u_{*_a} = \mathcal{P}^{1/2}u_{*_w}$, which was used to derive equation (2.11). For a smooth interface the turbulent kinetic energy and dissipation rate are zero at the interface. Rough interfaces are modelled by prescribing fixed values of turbulent kinetic energy and dissipation rate on either side of the interface. These values are determined from equations (A 2) and (A 3), which give values on the air side if $\mathcal{V} = \mathcal{P} = 1$, and values on the water side if $\mathcal{V} = v_w/v_a$ and $\mathcal{P} = \rho_w/\rho_a$.

Nine coupling conditions are necessary for the perturbed flow at the air–water interface. Continuity of velocity and shear stress at $Z = 0$ give

$$[U_1] = [V_1] = 0, \quad \left[\mathcal{P} \left(\frac{\mathcal{V}}{\mathcal{R}} + \bar{v}_{t_B} \right) \left(i\mathcal{K}V_1 + U'_1 - f'U'_B/\mathcal{K} \right) + \mathcal{P}\bar{v}_{t_1} U'_B \right] = 0, \tag{B2}$$

while continuity of normal stress yields

$$\left[-(P_1 + \mathcal{P}/(\mathcal{K}F^2)) + 2\mathcal{P} \left(\frac{\mathcal{V}}{\mathcal{R}} + \bar{v}_{t_B} \right) V'_1 \right] = 0 \text{ at } Z = 0. \tag{B3}$$

Continuity of normal stress involves a forcing, $\mathcal{P}/(\mathcal{K}F^2)$, where $F = u_{*_a}/(g\mathcal{L})^{1/2}$ is a Froude number, which arises from the coordinate transform since the pressure is defined relative to the mean water level. This forcing term drives the perturbation

flow. The mass conservation condition must be enforced across the interface, which yields

$$\left[i\mathscr{K} U_1 + V_1' - if U_B' \right] = 0 \text{ at } Z = 0. \tag{B 4}$$

The water surface roughness is held fixed along the wave surface so that K_1 and $\tilde{E}_1$ vanish in both the air and water at the interface. In the uncoupled flow, the wave speed C is a purely real quantity and is specified, but in the coupled flow, C is complex and is an eigenvalue of the solution, determined so that the solution satisfies the kinematic boundary condition, $V_1 = i(U_s - C)$. This requires some iteration on the wave speed as explained in §3.2.

REFERENCES

ABRAMS, J. & HANRATTY, T. J. 1985 Relaxation effects observed for turbulent flow over a wavy surface. *J. Fluid Mech.* **151**, 443–455.

AL-ZANAIDI, M. A. & HUI, W. H. 1984 Turbulent airflow over water waves – a numerical study. *J. Fluid Mech.* **148**, 225–246.

ASCE Task Committee on Turbulence Models in Hydraulic Computations 1988 Turbulence modeling of surface water flow and transport, Part I. *J. Hydraul. Engng* **114**, 970–991.

ASCHER, U. M., MATTHEIJ, R. M. M. & RUSSELL, R. D. 1988 *Numerical Solution of Boundary Value Problems for Ordinary Differential Equations.* Prentice Hall.

BELCHER, S. E., HARRIS, J. A. & STREET, R. L. 1994 Linear dynamics of wind waves in coupled turbulent air–water flow. Part 1. Theory. *J. Fluid Mech.* **271**, 119–151.

BELCHER, S. E., HARRIS, J. A. & STREET, R. L. 1995 Linear dynamics of wind-waves in coupled turbulent air-water flow. Part 3. Energy budget. *J. Fluid Mech.* (Submitted).

BELCHER, S. E. & HUNT, J. C. R. 1993 Turbulent shear flow over slowly moving waves. *J. Fluid Mech.* **251**, 109–148.

BELCHER, S. E., NEWLEY, T. M. J & HUNT, J. C. R. 1993 The drag on an undulating surface due to the flow of a turbulent boundary layer. *J. Fluid Mech.* **249**, 557–596.

BELJAARS, A. C. M., WALMSLEY, J. L. & TAYLOR, P. A. 1987 A mixed spectral finite difference model for neutrally-stratified boundary-layer flow over roughness change and topography. *Boundary-Layer Met.* **38**, 273–303.

CHALIKOV, D. V. & MAKIN, V. K. 1991 Models of the wave boundary layer. *Boundary-Layer Met.* **56**, 83–99.

CHEUNG, T. K. & STREET, R. L. 1988 The turbulent layer in the water at an air–water interface. *J. Fluid Mech.* **194**, 133–151.

GENT, P. R. 1977 A numerical model of the air flow above water waves. Part 2. *J. Fluid Mech.* **82**, 349–369.

GENT, P. R. & TAYLOR, P. A. 1976 A numerical model of the air flow above waves. *J. Fluid Mech.* **77**, 105–128.

HARRIS, J. A. 1992 On the growth of water waves and the motions beneath them. PhD Thesis, Stanford University.

HARRIS, J. A. & STREET, R. L. 1994 Numerical simulation of turbulent flow over a moving wavy boundary: Norris and Reynolds extended. *Phys. Fluids* **6**, 924–943.

HARRIS, J. A. & STREET, R. L. 1991 Solution of coupled mean flow profiles for a stratified two-phase flow using the k-epsilon turbulence model. In *Proc. Fourth Intl Symp. on Computational Fluid Dynamics, Davis, California.*

HSU, C. T., HSU, E. Y. & STREET, R. L. 1981 On the structure of turbulent flows over a progressive water wave: theory and experiment in a transformed, wave-following coordinate system. *J. Fluid Mech.* **105**, 87–117.

HSU, C. T. & HSU, E. Y. 1983 On the structure of turbulent flow over a progressive water wave: theory and experiment in a transformed wave-following coordinate system. Part 2. *J. Fluid Mech.* **131**, 123–153.

KONDO, J. 1976 Parameterization of turbulent transport in the top meter of the ocean. *J. Phys. Oceanogr.* **6**, 712–720.

LAUNDER, B. E. & SHARMA, B. I. 1974 Application of the energy dissipation model of turbulence to the calculation of a flow near a spinning disk. *Lett. Heat Mass Transfer* **1**, 131–138.

LAUNDER, B. E., REECE, G. T. & RODI, W. 1975 The development of a Reynolds stress turbulent closure. *J. Fluid Mech.* **68**, 537–566.

MILES, J. W. 1957 On the generation of surface waves by shear flows *J. Fluid Mech.* **3**, 185–204.

NEWLEY, T. M. J. 1986 Turbulent air flow over low hills. PhD thesis, University of Cambridge.

NORRIS, H. L. & REYNOLDS, W. C. 1975 Turbulent channel flow with a moving wavy boundary. *Tech. Rep.* TF-7. Dept. of Mechanical Engng, Stanford University.

PATEL, V. C., RODI, W. & SCHEUERER, G. 1985 Turbulence models for near-wall and low Reynolds number flows: A review. *AIAA J.* **23**, 1308–1319.

RILEY, D. S., DONELAN, M. A. & HUI, W. H. 1982 An extended Miles' theory for wave generation by wind. *Boundary-Layer Met.* **22**, 209–225.

SHEMDIN, O. H. 1976 Momentum transfer at the air-water interface. *AIChE, Symp. on Transport Processes in Lakes and Oceans, Atlantic City,* 263–284.

SNYDER, R. L., DOBSON, F. W., ELLIOT, J. A. & LONG, R. B. 1981 Array measurements of atmospheric pressure fluctuations above surface gravity waves. *J. Fluid Mech.* **102**, 1–59.

TOWNSEND, A. A. 1972 Flow in a deep turbulent boundary layer over a surface distorted by water waves. *J. Fluid Mech.* **55**, 719–735.

TOWNSEND, A. A. 1980 Sheared turbulence and additional distortion. *J. Fluid Mech.* **98**, 171–191.

WALMSLEY, J. L., TAYLOR, P. A. & KEITH, T. 1986 A simple model of neutrally stratified boundary layer flow over complex terrain with surface roughness modulations (MS3DJH/3R). *Boundary-Layer Met.* **36**, 157–186.

WOOD, N. & MASON, P. J. 1993 The pressure force induced by neutral turbulent flow over hills. *Q. J. R. Met. Soc.* **119**, 1233–1267.

XU, D. & TAYLOR, P. A. 1995 Boundary-Layer parameterisation of drag over smallscale topography. *Q. J. R. Met. Soc.* **121**, 433-443.

ZILKER, D. P. & HANRATTY, T. J. 1979 Influence of the amplitude of a solid wavy wall on a turbulent flow. Part 2. Separated flows. *J. Fluid Mech.* **90**, 257–271.